Electromechanical resonant ice protection systems: numerical investigation through a phase-field mixed adhesive/brittle fracture model

Alexis Marbœuf, Lokman Bennani, Marc Budinger, Valérie Pommier-Budinger

Electromechanical Resonant Ice Protection Systems: Numerical Investigation through a Phase-Field mixed Adhesive / Brittle Fracture Model

Alexis Marbœuf[a,b,*], Lokman Bennani[a], Marc Budinger[b], Valérie Pommier-Budinger[c]

[a] *ONERA / DMPE, Université de Toulouse F-31055 - France*
[b] *Institut Clément Ader, Université de Toulouse, CNRS-INSA-ISAE-Mines Albi-UPS, Toulouse 31400, France*
[c] *Institut Supérieur de l'Aéronautique et de l'Espace (ISAE SUPAERO), Université de Toulouse, Toulouse 31400, France*

Abstract

Electromechanical resonant de-icing systems provide a low-energy solution against ice accumulation on aircraft. Recent researches show a growing interest towards these systems in the context of more electrical aircraft. Electromechanical de-icing systems consists in electric actuators producing stress within the ice, through micro-vibrations of the surface to be protected, leading to bulk or adhesive failure and, ultimately, ice shedding. The understanding of the mechanisms at play is of prime importance in order to design efficient ice protection systems. Despite a large number of studies in the literature, there is still a lack when dealing with fracture propagation phenomena in this context. In this work the authors propose a model based on the well established phase-field variational approach to fracture. The approach is applied to the study of crack propagation and debonding of ice under the effect of an electromechanical resonant de-icing system. Numerical experiments are performed in order to assess possible ice shedding mechanisms.

Keywords: Electromechanical de-icing, Numerical modelling, Phase-field methods, Fracture mechanics, Adhesive debonding

1. Introduction

Icing has been identified as a severe issue since the beginning of aviation [1, 2]. It can occur both during flight and on ground. In flight, ice accretion is caused by supercooled droplets suspended in clouds. They impact the aircraft surfaces and freeze. Ice then accumulates on the surface which may lead to an increase of mass, the degradation of aerodynamic performances or engine damage/flameout due to ice ingestion.

Ice protection systems are then required to ensure aircraft safety [3]. Current strategies for anti-icing or de-icing can be chemical, thermal, mechanical or a combination of them [4, 5]. Of course, each of these strategies possesses their own drawbacks and advantages [6, Tab. 1] and the choice depends on the targeted applications. In the context of more electrical aircraft, electromechanical solutions are especially interesting for their potential in terms of weight, durability and energy savings. The basic idea consists in feeding the protected surface with vibrations by means of electric actuators. These vibrations generate stress within the ice leading to cohesive (bulk fracture) and adhesive (delamination) failures.

A large amount of work has been carried out to study the efficiency of electromechanical ice protection systems. In the low frequency range (Hertz), Venna *et al.* focused on energy and weight considerations either by using smart structures [7, 8] or by combining shear and impulse forces [9]. The de-icing power of waves in the megaHertz range has been addressed by Ramanathan *et al.* [10] or by Kalkowski *et al.* [11] through semi-analytical models and experiments. However, most of the studies and the main focus of the present work lie within the kiloHertz range. Experiments together with finite elements modeling—mainly conducted by Palacios, Overmeyer *et al.* [12–18] but

*Corresponding author.
Email addresses: alexis.marboeuf@onera.fr (Alexis Marbœuf), lokman.bennani@onera.fr (Lokman Bennani), mbudinge@insa-toulouse.fr (Marc Budinger), valerie.budinger@isae-supaero.fr (Valérie Pommier-Budinger)

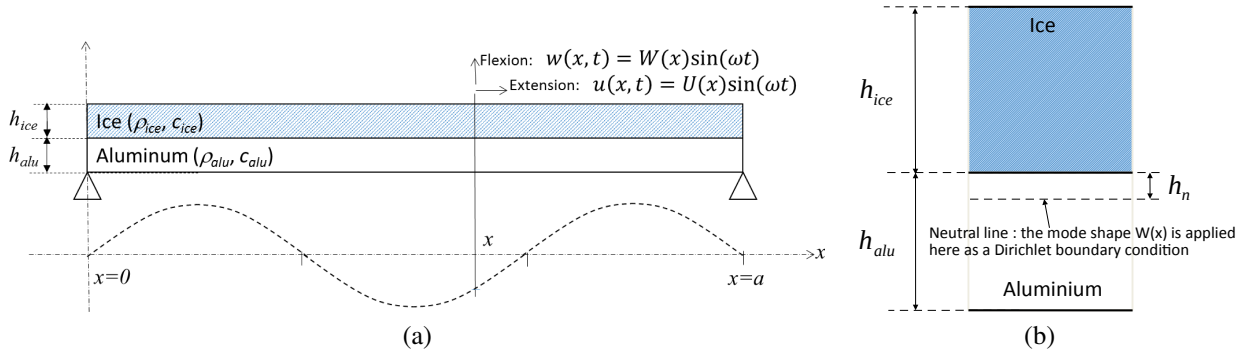

Figure 1: Electromechanical de-icing systems: (a) the analytic beam studied in [20, 22] and re-used in this paper as a test case; and (b) position h_n of the neutral line where the mode shape $W(x)$ is applied as a Dirichlet boundary condition.

also by Villeneuve *et al.* [19] or Strobl *et al.* [4] for an hybrid approach—showed the efficiency of ultrasonic de-icing at low-energy costs both on plates and helicopter rotor blades.

Nevertheless, there is still a lack of understanding concerning the mechanisms leading to the fracture and debonding of ice. Using beam theory, modal analysis and numerical tools, Budinger *et al.* provided a first step in this direction [20–22]. The resulting information was integrated into the design phase and guided the choice of vibrational modes. However, in their numerical analysis, Budinger *et al.* assumed *a priori* crack propagation and debonding mechanisms.

The goal of this paper is to assess the fracture mechanisms introduced by Budinger *et al.* [22]. To do so, a phase-field variational approach to fracture and adhesive debonding is used in order to fully simulate the shedding mechanism. The method allows to remove *a priori* assumptions on initation and propagation direction of fracture made in [22]. Our algorithm is tested on the analytical beam model of [22]. Knowing the variability of ice characteristics in literature, these results are only used to identify trends in the ice shedding process.

The paper is organized as follows: (i) Section 2 provides some details on electromechanical de-icing systems and re-introduces the analytical beam model and fracture mechanisms of [22]; (ii) Section 3 describes the mechanical modelling of cohesive and adhesive failure; (iii) Section 4 deals with the mechanical properties of ice and related issues; (iv) Section 5 is dedicated to the numerical results and related discussions; and (v) Section 6 concludes this paper and presents ongoing work.

2. Ice shedding mechanisms in electromechanical de-icing systems

2.1. Set up and assumptions

Budinger *et al.* [20, 22] modelled an electromechanical de-icing system by the configuration displayed in Figure 1(a), which is re-used in this paper as a test case. The aluminium support of length $a = 154$ mm, with simply supported boundary conditions, is covered by a layer of freezer ice—both of constant thicknesses $h_{alu} = 1.5$ mm and $h_{ice} = 2$ mm. Anti-icing mode of ice protection systems [23] or ice accretion models [24, 25] are thus not discussed here. Both the aluminium and the ice are considered as an elastic isotropic homogeneous material. Elastic coefficients for aluminium are set to $c_{alu} = 69$ GPa and $\nu_{alu} = 0.334$. Ice characterization is a more complex task and this is discussed in Section 4. Macroscopically, fracture is assumed to be: (i) brittle, which is justified for high strain rate [26]; and (ii) instantaneous. Shreurs [27] estimates the fracture propagation velocity in ice to be about 20 to 40 % of the speed of sound $v_s = \sqrt{c_{ice} / \rho}$, yielding $v \simeq 1000$ m / s.

Mode shapes are supposed to be identical to that of a uniform beam which undergoes in-plane extensional and out-of-plane flexural modes, essentially used in the literature. Investigation of the available analytical formulas in [22, Tab. 3]—derived from [28]—shows that pure extensional modes generate, at given frequency and magnitude, lower tensile stress at the top of the ice surface and lower shear stress at the ice / aluminium interface. Extensional modes also generally appear at higher frequencies (over 15 kHz) and thus: (i) require more energy; and (ii) may involve three-dimensional effects. Consequently, excitation of flexural modes—up to approximately 15 kHz—is privileged in this work. These modes write [22, Tab. 3]

$$w(x,t) = W(x)\sin(\omega t) = W_0 \sin\left(\frac{n\pi x}{a}\right)\sin(\omega t)\,. \tag{1}$$

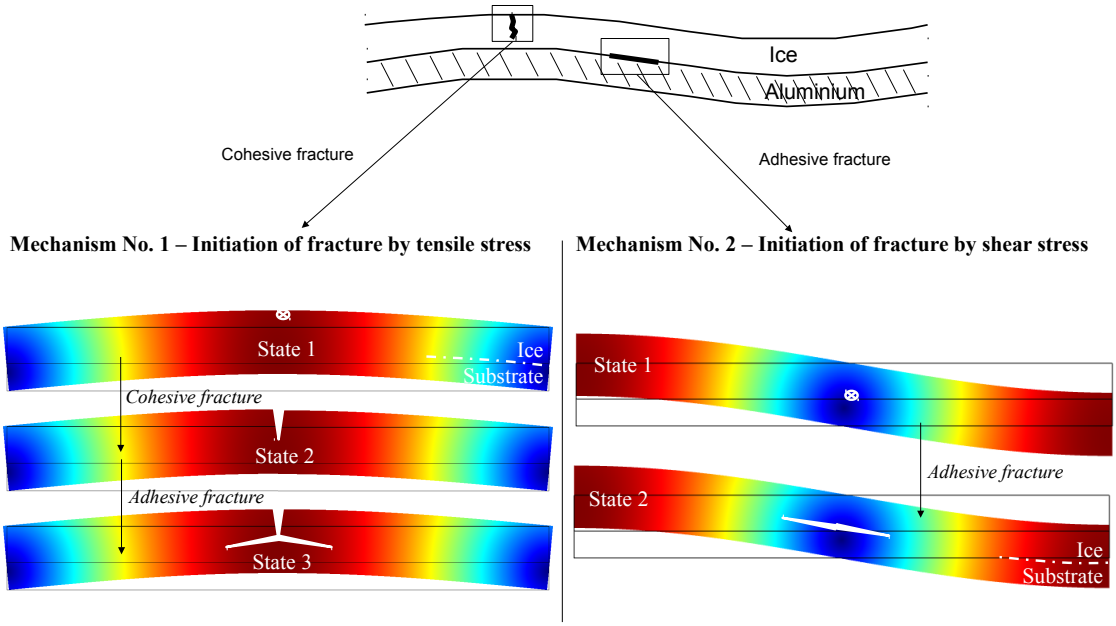

Figure 2: The two possible kinds of fracture: cohesive in the ice layer or adhesive (delamination) at the ice-substrate interface. Corresponding mechanisms postulated in [22] for delamination.

Refering to the estimation of the fracture propagation velocity, the characteristic time of fracture is negligible against the vibratory amplitude of modes under 40 kHz. Therefore, only the spatial part $W(x)$—*i.e.* the maximum amplitude of $w(x,t)$ in time—is retained here. According to the beam assumption, the flexural mode shape $W(x)$ is applied on the neutral line given by [22, Tab. 3]

$$h_n = \frac{1}{2}\frac{c_{alu}\,h_{alu}^2 - c_{ice}\,h_{ice}^2}{c_{alu}\,h_{alu} + c_{ice}\,h_{ice}}, \tag{2}$$

as described in Figure 1(b). This work is technology-independant and technology considerations [3] are not discussed in this paper.

The problem considered in this paper reduces to find a steady-state (fractured or not) compatible with the external load $W(x)$.

2.2. *Postulated ice shedding mechanisms*

Two ice shedding mechanisms are postulated by Budinger *et al.* in [22]. They are depicted in Figure 2 for flexural modes: maximum shear (resp. tensile) stress region is called a node (resp. an antinode) and is colored in blue (resp. red). Mechanism 1 corresponds to a cohesive fracture initiated by tensile stress at the top of the ice surface, propagating through the thickness and causing delamination thanks to a re-distribution of the stress at the ice/aluminium interface. In mechanism 2, the shear stress at the interface is sufficient to delaminate the ice, without cohesive failures. The energy balance approach for fracture propagation considered in [22] allows discriminating between the two mechanisms when flexural modes are applied: (i) initiation of a cohesive fracture and propagation through the entire ice thickness is possible at low frequencies but an adhesive damage (delamination) generally not follows and often requires higher magnitude (*i.e.* voltage); and (ii) mechanism 2 is unlikely to occur.

3. Mechanical modelling

This section presents the mechanical modelling considered in this paper, building upon previous work [29–31]. It includes both brittle fracture and adhesive debonding. These two phenomena are firstly discussed and modelled

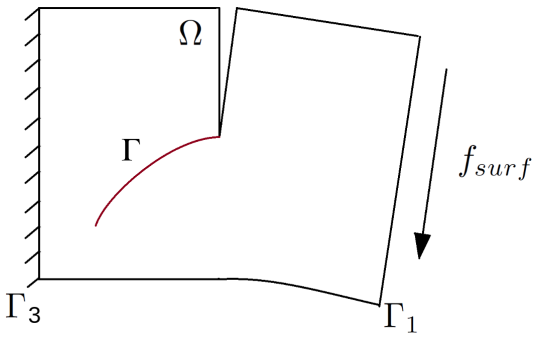

Figure 3: Illustration of a cracked material.

separately. The different terms involved in the model along with equations are introduced and justified. In a final step, all these terms are gathered and the full coupled model is derived. The resolution method closes the section.

3.1. Brittle fracture model

Modelling fracture mechanics is not an easy task. Several methods are available in the literature, *e.g.* XFEM [32–34], remeshing [35–37], Cohesive Zone Models [38–40] or Variational Approach [41, 42]. Concerning applications to ice, all these methods have been applied: both XFEM [43] and remeshing [44, 45] are used for modeling ice-floe/sea-ice fractures; Cohesive Zone Model have been successfully applied for sea-ice and structure interactions [46–48] but also for aircraft (or similar) applications [49, 50]; cohesive and adhesive failures of ice on an aluminium airfoil have been investigated thanks to a variational approach in the context of electrothermal de-icing systems [29–31]. Regarding electromechanical ice protection systems, Budinger *et al.* compared a computed energy release rate to a given fracture toughness, according to Griffith's theory [27], to determine if a fracture is unstable or not [22]. To the authors' knowledge, it is the only attempt to numerically study fracture propagation in this context. As an energy balance approach, the work of Budinger *et al.* took the same flavor as in [31] but assumed fracture mechanisms to be known.

The method described here falls into the concept of variationnal approaches [41, 42] and phase-field models [51–56]. Note that some authors combined this approach with other fracture methods such as remeshing [57]. The problem is formulated with an energy functional and relies on an energy conservation principle. The energy conservation principle translates the interplay between elastic energy E_{el} and crack surface energy E_Γ [58]. We consider a material Ω, cracked on the surface Γ, clamped on Γ_3 and undergoing an external force $\boldsymbol{f}_{surf}$ on Γ_1 such as in Figure 3. The model targets the balance between E_{el} and E_Γ for this particular configuration and thus predicts a steady state compatible with external loads applied on Γ_1 and Γ_3. As a phase-field model, the crack surface energy E_Γ—written in the form of a surface integral—is approximated by a volume integral E_{crack} through the introduction of a smooth scalar damage variable $d \in [0, 1]$ [52]

$$E_\Gamma = \int_\Gamma g_c \, d\Gamma \simeq \int_\Omega \phi(d\,,\, \boldsymbol{\nabla} d)\, dV = E_{crack}.$$

The variable d smoothly interpolates between broken states ($d = 1$) and unbroken states ($d = 0$), the width of the regularized crack being measured by a parameter ℓ.

The starting point of the model is elastic energy E_{el} and regularized crack surface energy E_{crack}

$$E_{el} = \int_\Omega \psi(\boldsymbol{\epsilon}\,,\, d)\, dV \text{ and } E_{crack} = \int_\Omega \phi(d\,,\, \boldsymbol{\nabla} d)\, dV. \tag{3}$$

According to [52, 59], the crack surface density function ϕ—approximating the Griffith's surface energy—is expressed as

$$\phi(d\,,\, \boldsymbol{\nabla} d) = \frac{g_c}{c_0}\left(\frac{1}{\ell}\,\alpha(d) + \ell\, \boldsymbol{\nabla} d \cdot \boldsymbol{\nabla} d\right) \text{ where } c_0 = 4\int_0^1 \sqrt{\alpha(s)}\, ds. \tag{4}$$

The "so-called" Γ-convergence [60–67] guarantees that the volume integral E_{crack}—with the crack density function ϕ given by (4)—actually converges toward the Griffith's surface energy E_Γ as the parameter ℓ goes to zero. If some difficulties can arise in practice [68], Γ-convergence results hold at least numerically [51, 59, 69]. Miehe *et al.* [51] propose to split the elastic density function into purely tensile ψ^+ and compressive ψ^- parts defined by using the eigenvalues of ϵ ($\epsilon_\star$ and $\epsilon_\square$ in two dimensions) and a positive/negative part function noted $< \ . \ >_\pm$

$$\psi^+(\boldsymbol{\epsilon}) = \tfrac{\lambda}{2} < \epsilon_\star + \epsilon_\square >_+^2 + \mu\,(< \epsilon_\star >_+^2 + < \epsilon_\square >_+^2) \tag{5}$$

$$\psi^-(\boldsymbol{\epsilon}) = \tfrac{\lambda}{2} < \epsilon_\star + \epsilon_\square >_-^2 + \mu\,(< \epsilon_\star >_-^2 + < \epsilon_\square >_-^2). \tag{6}$$

Only the tensile part contributes to crack nucleation or propagation. Consequently, ψ^+ is multiplied by a function $f_1(d)$ representing the degradation of this tensile part into crack surface energy

$$\psi(\boldsymbol{\epsilon}\,,\,d) = f_1(d)\,\psi^+(\boldsymbol{\epsilon}) + \psi^-(\boldsymbol{\epsilon}). \tag{7}$$

It now remains to define the geometric function α and the degradation function f_1, which have to satisfy the following requirements [52]

$$\alpha(0) = 0, \quad \alpha(1) = 1, \quad f_1(0) = 1, \quad f_1(1) = 0, \quad f_1'(1) = 0 \quad \text{and} \quad f_1'(d) < 0.$$

Many expressions exist for α and f_1: see for example [29–31, 51, 52, 70–72]. This choice greatly influences the model behavior but, in the general case, the strain-stress relation takes the following form: (i) an elastic phase from $(\epsilon\,,\,\sigma) = (0, 0)$ to $(\epsilon\,,\,\sigma) = (\epsilon_e\,,\,\sigma_e)$, where the damage remains 0 everywhere; (ii) an homogeneous damage phase from $(\epsilon\,,\,\sigma) = (\epsilon_e\,,\,\sigma_e)$ to $(\epsilon\,,\,\sigma) = (\epsilon_c\,,\,\sigma_c)$, where the damage increases but remains homogeneous in the domain; (iii) a damage localization phase from $(\epsilon\,,\,\sigma) = (\epsilon_c\,,\,\sigma_c)$ to $(\epsilon\,,\,\sigma) = (+\infty\,,\,0)$, where cracks appear and develop. Following [59, 73], the two functions α and f_1

$$\alpha(d) = d\,[\xi + (1-\xi)\,d]\,, \tag{8}$$

$$f_1(d) = \frac{(1-d)^p}{(1-d)^p + a_1\,d\,P(d)} \text{ and } P(d) = 1 + a_2\,d + a_2\,a_3\,d^2, \tag{9}$$

are adopted in this paper with

$$a_1 = \frac{2\,\xi\,c_{ice}\,g_c}{c_0\,\ell\,\sigma_c^2}, \tag{10}$$

$$\xi = 0.5, \quad p = 2, \quad a_2 = \tfrac{1}{\xi}\left[\left(-\tfrac{4\pi\xi^2}{c_0}\tfrac{g_c}{\sigma_c^2}\,k_0\right)^{2/3} + 1\right] - (p+1), \quad a_3 = \tfrac{1}{a_2}\left[\tfrac{1}{\xi}\left(\tfrac{c_0\,\omega_c\,\sigma_c}{2\pi\,g_c}\right)^2 - (1+a_2)\right], \tag{11}$$

where $k_0 = -\frac{\sigma_c^2}{2\,g_c}$ and $\omega_c = \frac{2\,g_c}{\sigma_c}$ are respectively the initial slope (B.7) and the ultimate crack opening (B.8) of a linear softening law. For this choice, there is no homogeneous damage phase—*i.e.* $\epsilon_e = \epsilon_c$ and $\sigma_e = \sigma_c$ denoted ϵ_c and σ_c in all the following. Cracks thus appear just after the elastic phase. Constitutive relations (8)-(9)-(10)-(11) present some advantages: (i) the presence of an elastic phase where $d = 0$ everywhere; (ii) a finite crack support in which $d > 0$ in the damage localization phase; and (iii) an ℓ-independant critical stress σ_c. Concerning the latter point, ℓ can be considered as a constant material parameter [70, 72] but the Γ-convergence is lost. Here, an ℓ-independant critical stress σ_c is achieved through Relation (10)—see Appendix B and [73] for more details. In this case, one can let the parameter ℓ go to zero in order to obtain sharper crack topology while maintaning the crack nucleation at the constant critical stress σ_c. The notion of Γ-convergence is retrieved and the parameter ℓ keeps its numerical role. Parameters $\xi = 0.5$ and $p = 2$ are related to the numerical stability of the proposed algorithm in Subsection 3.3 and to the boundedness of the damage variable d (Appendix A). Expressions for a_2 and a_3 are justified in Section 4. Now, the model only requires the material parameters g_c and σ_c to be fully determined, which are also discussed in Section 4.

Using variational arguments, one may show that

$$\begin{array}{ll}
-div\,(\boldsymbol{\sigma}(\boldsymbol{\epsilon}\,,\,d)) = \boldsymbol{f}_{vol} & \text{in } \Omega \\
\boldsymbol{\sigma}\cdot\boldsymbol{n} = \boldsymbol{f}_{surf} & \text{on } \Gamma_1 \\
\boldsymbol{u} = \boldsymbol{u}_d & \text{on } \Gamma_2 \\
\frac{g_c}{c_0\,\ell}\alpha'(d) - 2\,\frac{g_c\,\ell}{c_0}\Delta d = -f_1'(d)\,\psi^+(\boldsymbol{\epsilon}) & \text{in } \Omega \\
\boldsymbol{\nabla} d\cdot\boldsymbol{n} = 0 & \text{on } \partial\Omega
\end{array} \tag{12}$$

where the stress tensor $\boldsymbol{\sigma}$ is given by $\sigma = \frac{\partial \psi}{\partial \boldsymbol{\epsilon}}$. Note that $\boldsymbol{\sigma}$ is a non-linear function of $\boldsymbol{\epsilon}$ but also of the bulk damage d since $\psi = \psi(\boldsymbol{\epsilon}\,,\, d)$

$$\boldsymbol{\sigma} = \frac{\partial \psi}{\partial \boldsymbol{\epsilon}} = f_1(d)\left[\lambda < tr(\boldsymbol{\epsilon}) >_+ \mathbb{1} + 2\,\mu\,\boldsymbol{\epsilon}_+\right] + \left[\lambda < tr(\boldsymbol{\epsilon}) >_- \mathbb{1} + 2\,\mu\,\boldsymbol{\epsilon}_-\right]. \tag{13}$$

In addition, the right hand side $-f_1'(d)\,\psi^+(\boldsymbol{\epsilon})$ of the bulk damage equation that drives the damage growth is also non-linear here with respect to d. It represents an additional difficulty compared to many similar works where the choice $f_1(d) = (1-d)^2$—leading to a linear expression for $f_1'(d)$—is commonly made: see for example [29–31]. This will be discussed in the Subsection 3.3.

3.2. Adhesive debonding model

The model developped in this section is built upon [31, 74] with an approach akin to the bulk damage model of Subsection 3.1. The adhesive interface Γ_2 between two solids Ω_1 and Ω_2 is modelled by microscopic bonds as depicted in Figure 4. An adhesive damage variable β is introduced and plays the role of the bulk damage d: $\beta = 0$ means that the interface is intact while $\beta = 1$ means that the interface is completely broken. Considering no bulk damage both in Ω_1 and Ω_2, the total energy of the system is composed of the elastic energy $E_{el}^{\Omega_1}$ in Ω_1, the elastic energy $E_{el}^{\Omega_2}$ in Ω_2, the elastic energy stored in microscopic bonds E_{micro} and the surface energy E_{adh} associated with the debonding process. These energies are defined by

$$E_{el}^{\Omega_1} = \int_{\Omega_1} \psi_1(\boldsymbol{\epsilon_1})\,dV,\; E_{el}^{\Omega_2} = \int_{\Omega_2} \psi_2(\boldsymbol{\epsilon_2})\,dV,\; E_{micro} = \int_{\Gamma_2} \gamma(\beta\,,\,\boldsymbol{u}_1\,,\,\boldsymbol{u}_2)\,d\Gamma,\;\text{ and }\; E_{adh} = \int_{\Gamma_2} \phi_{adh}(\beta\,,\,\boldsymbol{u}_1\,,\,\boldsymbol{u}_2)\,d\Gamma. \tag{14}$$

As in the bulk damage model, energy accumulates in microscopic bonds and can be converted to surface energy in order to increase the adhesive damage β. The total work of external forces W_{ext} is written as the sum of the work of external forces acting on each part of the system taking seperately, *i.e.* $W_{ext} = W_{ext}^{\Omega_1} + W_{ext}^{\Omega_2} + W_{ext}^{\Gamma_2}$. The work $W_{ext}^{\Gamma_2}$ takes into account that the block Ω_1 produces a force reaction $-\boldsymbol{R}_1$ while Ω_2 produces the force reaction $-\boldsymbol{R}_2$ on the adhesive interface Γ_2. Equivalently, $W_{ext}^{\Omega_1}$ (resp. $W_{ext}^{\Omega_2}$) includes the effect produced by Γ_2 on Ω_1 (resp. Ω_2) since $\Gamma_2 \subset \partial\Omega_1$ (resp. $\Gamma_2 \subset \partial\Omega_2$). This effect reads $\boldsymbol{\sigma}_1 \cdot \boldsymbol{n}_1 = \boldsymbol{R}_1$ and $\boldsymbol{\sigma}_2 \cdot \boldsymbol{n}_2 = \boldsymbol{R}_2$ on Γ_2 by the action-reaction principle. The total work of external forces is thus expressed as

$$\begin{aligned} W_{ext} = &\underbrace{\int_{\Omega_1} \boldsymbol{f}_{vol}\cdot\delta\boldsymbol{u}_1\,dV + \int_{\partial\Omega_1} \boldsymbol{f}_{surf}\cdot\delta\boldsymbol{u}_1\,d\Gamma}_{W_{ext}^{\Omega_1}:\text{ external forces acting on }\Omega_1} + \underbrace{\int_{\Omega_2} \boldsymbol{f}_{vol}\cdot\delta\boldsymbol{u}_2\,dV + \int_{\partial\Omega_2} \boldsymbol{f}_{surf}\cdot\delta\boldsymbol{u}_2\,d\Gamma}_{W_{ext}^{\Omega_2}:\text{ external forces acting on }\Omega_2} \\ &+ \underbrace{\int_{\Gamma_2} (-\boldsymbol{R}_1)\cdot\delta\boldsymbol{u}_1\,d\Gamma + \int_{\Gamma_2} (-\boldsymbol{R}_2)\cdot\delta\boldsymbol{u}_2\,d\Gamma}_{W_{ext}^{\Gamma_2}:\text{ external forces acting on }\Gamma_2}. \end{aligned} \tag{15}$$

Again, for the configuration described in Figure 4, variational arguments lead to

$$\begin{array}{ll} -div\,(\boldsymbol{\sigma}_1(\boldsymbol{\epsilon}_1)) = \boldsymbol{f}_{vol} & \text{in } \Omega_1 \\ \boldsymbol{\sigma}_1\cdot\boldsymbol{n}_1 = \boldsymbol{f}_{surf} & \text{on } \Gamma_1 \\ \boldsymbol{\sigma}_1\cdot\boldsymbol{n}_1 = \boldsymbol{R}_1 = -\left(\frac{\partial\gamma}{\partial\boldsymbol{u}_1} + \frac{\partial\phi_{adh}}{\partial\boldsymbol{u}_1}\right) & \text{on } \Gamma_2 \\ -div\,(\boldsymbol{\sigma}_2(\boldsymbol{\epsilon}_2)) = \boldsymbol{f}_{vol} & \text{in } \Omega_2 \\ \boldsymbol{u}_2 = \boldsymbol{u}_d & \text{on } \Gamma_3 \\ \boldsymbol{\sigma}_2\cdot\boldsymbol{n}_2 = \boldsymbol{R}_2 = -\left(\frac{\partial\gamma}{\partial\boldsymbol{u}_2} + \frac{\partial\phi_{adh}}{\partial\boldsymbol{u}_2}\right) & \text{on } \Gamma_2 \\ \frac{\partial\phi_{adh}}{\partial\beta} = -\frac{\partial\gamma}{\partial\beta} & \text{on } \Gamma_2 \end{array} \tag{16}$$

where stress tensors $\boldsymbol{\sigma}_1$ and $\boldsymbol{\sigma}_2$ are related to elastic energies through $\boldsymbol{\sigma}_1 = \frac{\partial\psi_1}{\partial\boldsymbol{\epsilon}_1}$ and $\boldsymbol{\sigma}_2 = \frac{\partial\psi_2}{\partial\boldsymbol{\epsilon}_2}$. Above, the outward normal with respect to Ω_1 (resp. Ω_2) is denoted $\boldsymbol{n}_1$ (resp. $\boldsymbol{n}_2$).

As a first attempt using variational approaches in the context of electromechanical de-icing systems and knowing identification difficulties, the adhesive modelling is here firstly simplified and then improved step by step. Three adhesive models are considered and summarized in Tab. 1. The first one only takes into account Mode I failure.

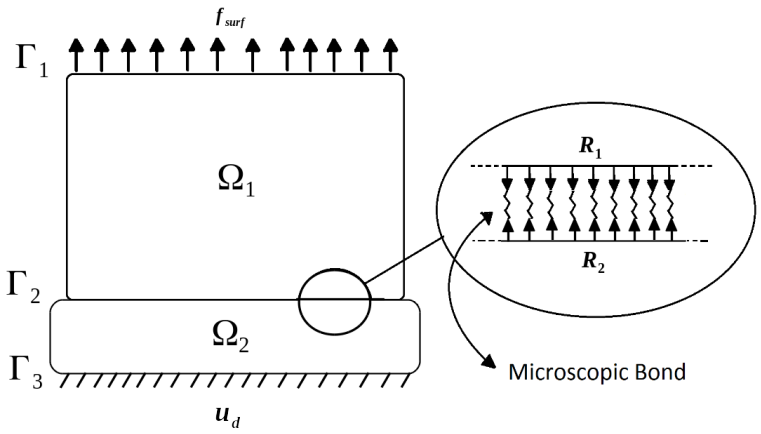

Figure 4: Two solids Ω_1 and Ω_2 with a common adhesive interface Γ_2 modelled by microscopic bonds.

However, according to Rice and Sih [75], the local stress at an interface between dissimilar materials presents both tensile and shear components, even when far-field loads are pure uniaxial tension (Mode I) or shear (Mode II). The consideration of pure Mode I failure seems therefore questionable [76] and models 2 and 3 presented below gradually include Mode II failure.

Model 1. The adhesive surface energy ϕ_{adh} is defined by analogy with the bulk damage model [31]

$$\phi_{adh}(\beta\,,\,\boldsymbol{u}_1\,,\,\boldsymbol{u}_2) = \phi_{adh}(\beta) = g_c^{adh}\,\beta^2. \tag{17}$$

The microscopic density energy γ writes [31]

$$\gamma(\beta\,,\,\boldsymbol{u}_1\,,\,\boldsymbol{u}_2) = f_2(\beta)\,\underbrace{\tfrac{k}{2}<[\![\boldsymbol{u}]\!]_n>_+^2}_{\gamma_\beta} + \underbrace{\tfrac{k_\infty}{2}\left[<[\![\boldsymbol{u}]\!]_n>_-^2 + [\![\boldsymbol{u}]\!]_\tau^2\right]}_{\gamma_0}. \tag{18}$$

In the above relation, $f_2(\beta) = (1-\beta)^2$ is the adhesive degradation function, $[\![\boldsymbol{u}]\!] = \boldsymbol{u}_2 - \boldsymbol{u}_1$ is the displacement jump across Γ_2 and $[\![\boldsymbol{u}]\!]_n$ (resp. $[\![\boldsymbol{u}]\!]_\tau$) its normal (resp. tangential) component. The microscopic density function (18) shares some similarities with the bulk elastic energy ψ: (i) its decomposition into two parts γ_β and γ_0; (ii) only one part—γ_β—participates to the debonding process; and (iii) the multiplication of this part by the degradation function f_2. Only Mode I failure is here taken into account: only the positive part of $[\![\boldsymbol{u}]\!]_n$ can be degraded into crack surface energy. The negative part of $[\![\boldsymbol{u}]\!]_n$ and the tangential part $[\![\boldsymbol{u}]\!]_\tau$ are strongly penalized thanks to a numerically infinite stiffness k_∞ setting to $k_\infty = 10^{17}$ Pa / m in this paper. The penalization of $<[\![\boldsymbol{u}]\!]_n>_-$ with a strong—or infinite—stiffness is a simple but common practice [77–81] to avoid inter-penetration. Note that in that case where $\phi_{adh}(\beta\,,\,\boldsymbol{u}_1\,,\,\boldsymbol{u}_2) = \phi_{adh}(\beta)$, adhesive boundary conditions on Γ_2—see Eqs (16)—simplify into $\boldsymbol{\sigma}_i\cdot\boldsymbol{n}_i = \boldsymbol{R}_i = -\frac{\partial\gamma}{\partial\boldsymbol{u}_i}$, $i = 1, 2$. Model 1 only requires a normal stiffness k as parameter. It will be related to an adhesive critical stress σ_c^{adh} for its computation in Section 4.

Model 2. Stored elastic energy γ through shear displacements jump $[\![\boldsymbol{u}]\!]_\tau$ can now feed the crack surface energy ϕ_{adh} and is therefore incorporated into γ_β. The adhesive crack energy ϕ_{adh} is kept isotropic. Model 2 consists in taking

$$\phi_{adh}(\beta\,,\,\boldsymbol{u}_1\,,\,\boldsymbol{u}_2) = \phi_{adh}(\beta) = g_c^{adh}\,\beta^2, \tag{19}$$

$$\gamma(\beta\,,\,\boldsymbol{u}_1\,,\,\boldsymbol{u}_2) = f_2(\beta)\,\underbrace{\tfrac{k}{2}\left[<[\![\boldsymbol{u}]\!]_n>_+^2 + \alpha_\tau\,[\![\boldsymbol{u}]\!]_\tau^2\right]}_{\gamma_\beta} + \underbrace{\tfrac{k_\infty}{2}<[\![\boldsymbol{u}]\!]_n>_-^2}_{\gamma_0}, \tag{20}$$

where $\alpha_\tau = \frac{k_\tau}{k}$. Again, an isotropic adhesive critical energy g_c^{adh} simplifies adhesive boundary conditions on Γ_2. The introduced tangential stiffness k_τ is much more difficult to calibrate than the normal one and its computation requires additional modelisation choices coming with additional uncertainties—see for example mixed-mode modelling in Cohesive Zone Model [82–85]. For that reason, the effect of the tangential component $[\![\boldsymbol{u}]\!]_\tau$ will be investigated by a sensitivity study on the parameter α_τ in Section 5.

Adhesive model	Stored energy γ in microscopic bonds	Fracture energy ϕ_{adh}
Model 1	Eq. (18): → Penalized tangential disp. jump for Mode II → Only the positive part of disp. jump participates to debonding: only Mode I failure	Eq. (17): isotropic
Model 2	Eq. (20): → Tangential disp. jump including in the debonding process: Mode I and II failure	Eq. (19): isotropic
Model 3	Eq. (22): → Tangential disp. jump including in the debonding process: Mode I and II failure	Eq. (21): anisotropic → Mode I and II distinction through $[\![\boldsymbol{u}]\!]$

Table 1: Summary of the three different adhesive models considered in this paper.

Model 3. Model 3 adds the possibility of a different adhesion energy, denoted $g_c^{adh,II}$, for Mode II failure. The adhesive energy release rate g_c^{adh} in ϕ_{adh} now depends on displacements $\boldsymbol{u}_1$ and $\boldsymbol{u}_2$ in order to split the source term γ_β/g_c^{adh} for the adhesive damage β into two contributions [86]. In other words $g_c^{adh} = g_c^{adh}(\boldsymbol{u}_1\,,\,\boldsymbol{u}_2)$ is chosen so that $\frac{\gamma_\beta}{g_c^{adh}}$ becomes $\frac{\gamma_\beta^I}{g_c^{adh}} + \frac{\gamma_\beta^{II}}{g_c^{adh,II}}$ where $\gamma_\beta^I = \frac{k}{2} < [\![\boldsymbol{u}]\!]_n >_+^2$ and $\gamma_\beta^{II} = \frac{k}{2}\,\alpha_\tau\,[\![\boldsymbol{u}]\!]_\tau^2$. Model 3 is obtained by

$$\phi_{adh}(\beta\,,\,\boldsymbol{u}_1\,,\,\boldsymbol{u}_2) = g_c^{adh}(\boldsymbol{u}_1\,,\,\boldsymbol{u}_2)\beta^2, \tag{21}$$

$$\gamma(\beta\,,\,\boldsymbol{u}_1\,,\,\boldsymbol{u}_2) = f_2(\beta)\underbrace{\tfrac{k}{2}\left[< [\![\boldsymbol{u}]\!]_n >_+^2 + \alpha_\tau\,[\![\boldsymbol{u}]\!]_\tau^2\right]}_{\gamma_\beta} + \underbrace{\tfrac{k_\infty}{2} < [\![\boldsymbol{u}]\!]_n >_-^2}_{\gamma_0}, \tag{22}$$

with

$$g_c^{adh}(\boldsymbol{u}_1\,,\,\boldsymbol{u}_2) = \gamma_\beta \,/\, \left(\frac{\gamma_\beta^I}{g_c^{adh}} + \frac{\gamma_\beta^{II}}{g_c^{adh,II}}\right). \tag{23}$$

The microscopic energy γ (22) is left unchanged with respect to Model 2 and a sensitivity study on α_τ will also be performed in Section 5. The question of the computation of the new introduced adhesion energy $g_c^{adh,II}$ is raised and we are facing the same issue as for α_τ. In this paper, as an illustration and to provide numerical results, the adhesive critical energy release rate $g_c^{adh,II}$ is computed with $g_c^{adh,II} = 10\,g_c^{adh}$ as in [86].

It seems finally useful to recall the expression of the adhesive damage β holding on the adhesive interface Γ_2 [31]. Whatever the adhesive model chosen, the last relation of (16) allows the direct computation of β

$$\beta = \frac{\gamma_\beta}{g_c^{adh} + \gamma_\beta}. \tag{24}$$

Since g_c^{adh} and γ_β are positive, the boundedness of β is trivial, *i.e.* $0 \leq \beta \leq 1$. For Model 3, the dependance $g_c^{adh}(\boldsymbol{u}_1\,,\,\boldsymbol{u}_2)$ is omitted in Eq. (24) and in all the following for simplicity but it has to be kept in mind. Appendix C details the computation of adhesive boundary conditions on Γ_2 in Eqs (16).

3.3. Coupled adhesive / brittle failure model

At this stage, all energies have been introduced and the complete coupled adhesive / brittle failure model can be derived. This derivation is briefly detailed in Appendix D to highlight that the coupling is only done through the variational principle.

Restarting from the configuration of Figure 4, we consider this time Dirichlet and Neumann boundary conditions both in Ω_1 and Ω_2 for generality. The block Ω_1 can undergo brittle failures while no bulk damage is considered in Ω_2. The boundary $\partial\Omega_1$ is decomposed into $\partial\Omega_1 = \Gamma_1^{\Omega_1} \cup \Gamma_2 \cup \Gamma_3^{\Omega_1}$ where $\Gamma_1^{\Omega_1}$ supports Neumann boundary condition

$\boldsymbol{\sigma}_1 \cdot \boldsymbol{n}_1 = \boldsymbol{f}_{surf}$, $\Gamma_3^{\Omega_1}$ supports Dirichlet boundary condition $\boldsymbol{u}_1 = \boldsymbol{u}_d$ and Γ_2 is the common adhesive interface with Ω_2. Of course, the same is done for $\partial\Omega_2$: $\partial\Omega_2 = \Gamma_1^{\Omega_2} \cup \Gamma_2 \cup \Gamma_3^{\Omega_2}$. The total energy of the system writes

$$E_{tot} = \underbrace{\int_{\Omega_1} \psi_1(\boldsymbol{\epsilon}_1\,,\, d)\, dV}_{E_{el}^{\Omega_1}} + \underbrace{\int_{\Omega_1} \phi(d\,,\, \boldsymbol{\nabla} d)\, dV}_{E_{crack}} + \underbrace{\int_{\Omega_2} \psi_2(\boldsymbol{\epsilon}_2)\, dV}_{E_{el}^{\Omega_2}} + \underbrace{\int_{\Gamma_2} \phi_{adh}(\beta\,,\, \boldsymbol{u}_1\,,\, \boldsymbol{u}_2)\, d\Gamma}_{E_{adh}} + \underbrace{\int_{\Gamma_2} \gamma(\beta\,,\, \boldsymbol{u}_1\,,\, \boldsymbol{u}_2)\, d\Gamma}_{E_{micro}}. \quad (25)$$

Using variational arguments on the energy E_{tot} (25), one gets the complete set of equations to be solved

$$\begin{array}{lll}
-div(\boldsymbol{\sigma}_1(\boldsymbol{\epsilon}_1\,,\, d)) = \boldsymbol{f}_{vol} & \text{in} & \Omega_1 \\
\boldsymbol{\sigma}_1 \cdot \boldsymbol{n}_1 = \boldsymbol{f}_{surf} & \text{on} & \Gamma_1^{\Omega_1} \\
\boldsymbol{u}_1 = \boldsymbol{u}_d & \text{on} & \Gamma_3^{\Omega_1} \\
\boldsymbol{\sigma}_1 \cdot \boldsymbol{n}_1 = \boldsymbol{R}_1 = -\left(\frac{\partial \gamma}{\partial \boldsymbol{u}_1} + \frac{\partial \phi_{adh}}{\partial \boldsymbol{u}_1}\right) & \text{on} & \Gamma_2 \\
\frac{g_c}{c_0\,\ell}\,\alpha'(d) - 2\,\frac{g_c\,\ell}{c_0}\,\Delta d = -f_1'(d)\,\psi_0^+(\boldsymbol{\epsilon}_1) & \text{in} & \Omega_1 \\
\boldsymbol{\nabla} d \cdot \boldsymbol{n}_1 = 0 & \text{on} & \partial\Omega_1 \\
\beta = \frac{\gamma_\beta}{g_c^{adh} + \gamma_\beta} & \text{on} & \Gamma_2 \\
-div(\boldsymbol{\sigma}_2(\boldsymbol{\epsilon}_2)) = \boldsymbol{f}_{vol} & \text{in} & \Omega_2 \\
\boldsymbol{\sigma}_2 \cdot \boldsymbol{n}_2 = \boldsymbol{f}_{surf} & \text{on} & \Gamma_1^{\Omega_2} \\
\boldsymbol{u}_2 = \boldsymbol{u}_d & \text{on} & \Gamma_3^{\Omega_2} \\
\boldsymbol{\sigma}_2 \cdot \boldsymbol{n}_2 = \boldsymbol{R}_2 = -\left(\frac{\partial \gamma}{\partial \boldsymbol{u}_2} + \frac{\partial \phi_{adh}}{\partial \boldsymbol{u}_2}\right) & \text{on} & \Gamma_2
\end{array} \quad (26)$$

Before we proceed to the algorithm description, the bulk damage equation in (26) is modified. First of all, one can introduce the expression of α' coming from (8)

$$2\,(1-\xi)\,\frac{g_c}{c_0\,\ell}\,d - 2\,\frac{g_c\,\ell}{c_0}\,\Delta d = -f_1'(d)\,\psi_0^+(\boldsymbol{\epsilon}_1) - \frac{g_c}{c_0\,\ell}\,\xi. \quad (27)$$

As remarked in Subsection 3.1, f_1' is here non-linear. Anticipating the linearization of the system (26), f_1' is written under the form $f_1'(d) = K(d)\,(d-1)$ where $K(d) \geq 0$. Eq. (27) becomes

$$\underbrace{\left[2\,(1-\xi)\,\frac{g_c}{c_0\,\ell} + K(d)\,\psi_0^+(\boldsymbol{\epsilon}_1)\right]}_{A}\, d - 2\,\frac{g_c\,\ell}{c_0}\,\Delta d = \underbrace{K(d)\,\psi_0^+(\boldsymbol{\epsilon}_1) - \frac{g_c}{c_0\,\ell}\,\xi}_{B}. \quad (28)$$

The iterative Algorithm 1 is implemented to solve the system (26). In this paper, the difference between two successive iterations for both the adhesive and cohesive damages serves as a stopping criterion. Tolerances ϵ_β and ϵ_d are set to 10^{-3}. It should be noted that equilibrium equations cannot be solved independently in Ω_1 and in Ω_2: displacements $\boldsymbol{u}_1$ and $\boldsymbol{u}_2$ are coupled through the boundary condition on Γ_2 since $\frac{\partial \gamma}{\partial \boldsymbol{u}_1}$, $\frac{\partial \phi_{adh}}{\partial \boldsymbol{u}_1}$, $\frac{\partial \gamma}{\partial \boldsymbol{u}_2}$ and $\frac{\partial \phi_{adh}}{\partial \boldsymbol{u}_2}$ depend both on displacements $\boldsymbol{u}_1$ and $\boldsymbol{u}_2$. Following Miehe *et al.* [51], the irreversibility is introduced through the history fields $\mathcal{H}_d$ and $\mathcal{H}_\beta$—respectively retaining the maximum of stored energies ψ_0^+ and γ_β throughout iterations. Non-linear terms are linearized taking advantage of the iterative resolution. For an iteration i: (i) the function $K(d)$ coming from f_1'—see Eq. (28)—depends on d^{i-1}; (ii) stress tensors $\boldsymbol{\sigma}_1$ and $\boldsymbol{\sigma}_2$ also depend on $\boldsymbol{\epsilon}^{i-1}$—see [31, Appendix B]; and (iii) the current displacement jump $[\![\boldsymbol{u}^i]\!]$ is replaced by the old one $[\![\boldsymbol{u}^{i-1}]\!]$ for the computation of F in adhesive boundary conditions on Γ_2 [31]. Computation of the damage, the mechanical equilibrium and adhesive boundary conditions through Eqs. (31) and (32) are therefore not equivalent to their counterpart in Eqs (26). Function F is given in Appendix C by Eq. (C.2) and has to be simplified depending on the considered adhesive modelling. It should be noted that Eq. (28) does not guarantee the boundedness of the damage variable d, *i.e.* $0 \leq d \leq 1$. Following Appendix A, a theoritical sufficient condition for $0 \leq d \leq 1$ is given by (A.4):

$$\underbrace{2\,(1-\xi)\,\frac{g_c}{c_0\,\ell} + K\,\mathcal{H}_d}_{\text{Term A}} \geq 0 \text{ and } \underbrace{K\,\mathcal{H}_d - \frac{g_c}{c_0\,\ell}\,\xi}_{\text{Term B}} \geq 0$$

Term A is always positive with $\xi = 0.5$ since $K\,\mathcal{H}_d \geq 0$ and $\frac{g_c}{c_0\,\ell} \geq 0$. Term B—playing the role of the damage source term—is slightly modified to stay positive. The bulk damage variable d^i for the iteration i is thus computed as follows

$$\left[2\,(1-\xi)\,\frac{g_c}{c_0\,\ell} + K(d^{i-1})\,\mathcal{H}_d^i\right] d^i - 2\,\frac{g_c\,\ell}{c_0}\,\Delta d^i = \max\left(0\,,\, K(d^{i-1})\,\mathcal{H}_d^i - \frac{g_c}{c_0\,\ell}\,\xi\right). \quad (29)$$

Numerically, in addition with conditions (A.4), one also needs that meshes do not present angles superior to 90° [30, 31]. In all numerical results of Section 5, mesh's quality is not checked and the damage variable d is observed to stay strictly positive but exceeds the upper bound only very slightly (effect on the third decimal).

Algorithm 1: Adhesive / brittle failure computation

initialization : perform a purely elastic computation (no adhesive or bulk damage);
while $\|\beta^i - \beta^{i-1}\|_\infty < \epsilon_\beta$ **and** $\|d^i - d^{i-1}\|_\infty < \epsilon_d$ **do**

Compute history fields;

$$\mathcal{H}_d^i = \max\left(\mathcal{H}_d^{i-1}\,,\,\psi_0^+(\boldsymbol{\epsilon}_1^{i-1})\right) \text{ in } \Omega_1 \text{ and } \mathcal{H}_\beta^i = \max\left(\mathcal{H}_\beta^{i-1}\,,\,\gamma_\beta([\![\boldsymbol{u}^{i-1}]\!])\right) \text{ on } \Gamma_2 \tag{30}$$

Solve the bulk damage Eq. (29) in Ω_1 and compute the adhesive damage on Γ_2 with (24) ;

$$\begin{array}{ll} \left[2\,(1-\xi)\,\frac{g_c}{c_0\,\ell} + K(d^{i-1})\,\mathcal{H}_d^i\right] d^i - 2\,\frac{g_c\,\ell}{c_0}\Delta d^i = \max\left(0\,,\,K(d^{i-1})\,\mathcal{H}_d^i - \frac{g_c}{c_0\,\ell}\xi\right) & \text{in } \Omega_1 \\ \boldsymbol{\nabla} d^i \cdot \boldsymbol{n}_1 = 0 & \text{on } \partial\Omega_1 \\ \beta^i = \frac{\mathcal{H}_\beta^i}{g_c^{adh} + \mathcal{H}_\beta^i} & \text{on } \Gamma_2 \end{array} \tag{31}$$

Solve the mechanical equilibrium in Ω_1 and Ω_2;

$$\begin{array}{llll} -div\left(\boldsymbol{\sigma}_1(\boldsymbol{\epsilon}_1^i\,,\,\boldsymbol{\epsilon}_1^{i-1}\,,\,d^i)\right) = \boldsymbol{f}_{vol} & \text{in } \Omega_1 & -div\left(\boldsymbol{\sigma}_2(\boldsymbol{\epsilon}_2^i\,,\,\boldsymbol{\epsilon}_2^{i-1})\right) = \boldsymbol{f}_{vol} & \text{in } \Omega_2 \\ \boldsymbol{\sigma}_1^i \cdot \boldsymbol{n}_1 = \boldsymbol{f}_{sur} & \text{on } \Gamma_1^{\Omega_1} & \boldsymbol{\sigma}_2^i \cdot \boldsymbol{n}_2 = \boldsymbol{f}_{sur} & \text{on } \Gamma_1^{\Omega_2} \\ \boldsymbol{u}_1^i = \boldsymbol{u}_d & \text{on } \Gamma_3^{\Omega_1} & \boldsymbol{u}_2^i = \boldsymbol{u}_d & \text{on } \Gamma_3^{\Omega_2} \\ \boldsymbol{\sigma}_1^i \cdot \boldsymbol{n}_1 = -F\left(\beta^i\,,\,[\![\boldsymbol{u}^{i-1}]\!]\right)[\![\boldsymbol{u}^i]\!] & \text{and} & \boldsymbol{\sigma}_2^i \cdot \boldsymbol{n}_2 = F\left(\beta^i\,,\,[\![\boldsymbol{u}^{i-1}]\!]\right)[\![\boldsymbol{u}^i]\!] & \text{on } \Gamma_2 \end{array} \tag{32}$$

end

The two full linear problems (31) and (32) can now be solved by classical finite element methods [29, 31]. In particular, $\mathbb{P}_1$ Lagrange shape functions are considered on unstructured triangular meshes and a direct LU solver is applied on resulting linear systems.

In Algorithm 1, cohesive and adhesive damages are coupled: the damage state d near the adhesive interface influences the adhesive damage β and, conversely, so does β on d. It couples cohesive and adhesive variables d and β only through displacements $\boldsymbol{u}$—more precisely through displacement jumps $[\![\boldsymbol{u}]\!]$ across the adhesive interface Γ_2. In particular, the adhesive interface keeps the same energy release rates g_c^{adh}, $g_c^{adh,II}$ and the same stiffnesses k, $\alpha_\tau = {}^{k_\tau}/_{k}$ whatever the damage state d. It would be very interesting to discuss the influence of d and β on each other together with more sophisticated coupling. However, such studies are beyond the scope of the present paper and postponed to later publications.

To close this section, it seems relevant to discuss the parameters ξ and p for brittle fracture summarized in Section 3.1. Our choice strongly relies on the resolution method described here. The value $p = 2$ is not only largely used in literature [59, Remark 2.3], it is also the choice that leads to a better numerical stability for (31). Wu shows in [59] that this parameter heavily affects the stress softening behavior in the damage localization phase. Once p is fixed, a_2 and a_3 therefore follow to fit the classical corresponding softening law (see Section 4 and Appendix B). The geometric parameter ξ—restricted to $\xi \in]0, 2]$ [59, 73]—is finally constrained by $\xi \leq 1$ as it guarantees that term A in (A.4) is positive for the boundedness of d—see Appendix A. Note that the value $\xi = 0$, discussed for example in [29–31, 42, 51, 52, 59, 70, 72, 87], is excluded since it lacks an initial elastic phase [73]. Among choices already considered in literature, it thus only remains $\xi = 0.5$ [42, 59, 70] and $\xi = 1$ [59, 70–72, 87]. A lower numerical stability of (31) is observed for $\xi = 1$ compared to $\xi = 0.5$, with $p = 2$, justifying the choice $\xi = 0.5$. The recommendation of Wu [59] to take the larger value $\xi = 2$ is therefore not followed in this paper. This value $\xi = 2$ allows satisfying an irreversibility condition on the crack bandwidth in a 1D homogeneous framework: the crack bandwidth cannot shrink. Here, the irreversibility is forced by the history function whatever the value of ξ and the crack bandwidth cannot effectively shrink.

Parameter	Value
Young's modulus c_{ice}	9.3 GPa
Poisson's ratio ν_{ice}	0.325

Parameter	Cohesive	Adhesive (ice/aluminium)
Strength σ_c	3 MPa	1 MPa
Critical energy release rate g_c	1 J / m^2	0.5 J / m^2

Table 2: Elastic coefficients, cohesive and adhesive properties for freezer ice [22] used in this paper.

4. Mechanical properties of ice

Our proposed mechanical modelling requires the knowledge of ice characteristics. As mentioned in Section 2, macroscopically, a brittle behaviour is observed for high strain rate [26]. To provide numerical results, the following classical parameters are needed: ice Young's modulus c_{ice}, ice Poisson's ratio ν_{ice}, cohesive critical energy release rate g_c, adhesive energy g_c^{adh}, cohesive critical strength σ_c and adhesive critical strength σ_c^{adh}. These parameters may vary considerably in literature [24, 25, 50, 88–94] depending on the type of ice (glaze or rime), the means to obtain this ice (freezer or wind tunnel), the type of degradation (cohesive or adhesive) and the interface material. Identification is a huge area of research in itself and uncertainties related to these parameters are beyond the scope of this paper, although the authors are fully aware of them. As an example, a recent review of ice adhesion on solid substrates [94] gathered 113 papers and concluded that results agreed within two or three order of magnitude on the adhesive critical strength σ_c^{adh} at given temperature—other critical values such as roughness are more poorly determined. A similar issue arises for the cohesive critical material strength σ_c which is introduced in the brittle fracture model through the Relation (10) in Subsection 3.1, derived in a uniaxial homogeneous case. Ideally, the value of σ_c should be identified on a test where an accurate measurement of the local stress in the nucleation zone can be performed: see for example the PIED (*Pour Identifier l'Endommagement Diffus*) test for concrete [95], reproducing uniaxial and homogeneous conditions. To the author's knowledge, such tests for the ice do not exist yet in the literature and we use the critical material strength σ_c given by Budinger *et al.* [22]. The other parameters previously mentioned are also provided in [22]: see Tab. 2. Keeping in mind the high scattering of materials' parameters in literature, values of Tab. 2 are no exception but it should be mentioned that results given in Section 5 are only used to highlight ice shedding trends. Then, these trends are only compared with postulated fracture mechanisms of [22]. Close comparisons with experimental results are excluded in this paper. Now, all parameters required by the model are not directly given by Budinger *et al.* in [22]. Some of them need to be related with the values of Tab. 2.

Brittle fracture parameters. In addition with ice parameters already given in Tab. 2, the model described in Subsection 3.1 needs the computation of ℓ, p, ξ, a_1, a_2 and a_3. Values of ℓ, p, ξ, and a_1 are already justified in Subsections 3.1 and 3.3. The focus is here on a_2 and a_3 which are related to the classical ice properties of Tab. 2. To that end, the approach of Wu [59] is followed and briefly described in Appendix B: (i) the equivalent Cohesive Zone Model of the phase-field variational approach to brittle fracture is formulated; (ii) the initial slope k_0 and the ultimate crack opening ω_c of the Cohesive Zone Model are expressed; (iii) parameters a_2 and a_3 are deduced from k_0 and ω_c; and (iv) a softening law is chosen (depending on the parameter p) fixing the pair $(k_0\,,\,\omega_c)$ and thus $(a_2\,,\,a_3)$. For $p=2$, we get Relations (B.6)

$$a_2 = \frac{1}{\xi}\left[\left(-\frac{4\pi\xi^2}{c_0}\frac{g_c}{\sigma_c^2}k_0\right)^{2/3}+1\right]-(p+1), \quad \text{and} \quad a_3 = \frac{1}{a_2}\left[\frac{1}{\xi}\left(\frac{c_0\,\omega_c\,\sigma_c}{2\pi\,g_c}\right)^2-(1+a_2)\right],$$

where $k_0 = -\frac{\sigma_c^2}{2\,g_c}$ and $\omega_c = \frac{2\,g_c}{\sigma_c}$ are respectively the initial slope (B.7) and the ultimate crack opening (B.8) of a linear softening law.

Adhesive parameters. Whatever the adhesive modelling, the normal stiffness k of microscopic bonds and the adhesive energy g_c^{adh} for Mode I failure are needed. Models 2 and 3 respectively add the ratio $\alpha_\tau = \frac{k_\tau}{k}$ and the adhesive energy $g_c^{adh,II}$ for Mode II failure. A sensitivity study is performed on α_τ. Mode I adhesion energy g_c^{adh} is given in Tab. 2 while $g_c^{adh,II} = 10\,g_c^{adh} = 5$ J / m^2 is chosen [86] as an illustration in order to provide numerical results. Finally, the computation of the normal stiffness k is performed thanks to a pure one-dimensional adhesive traction test such as in Figure 4 and described in Appendix E. Adhesive Model 1 is considered. In that case, adhesive boundary conditions explicited in Appendix C simplify into

$$\sigma\left(\llbracket u \rrbracket\right) = R_1 = -\frac{\partial\gamma}{\partial u_1} = -R_2 = \frac{\partial\gamma}{\partial u_2} = k\,(1-\beta)^2\,\llbracket u \rrbracket. \tag{33}$$

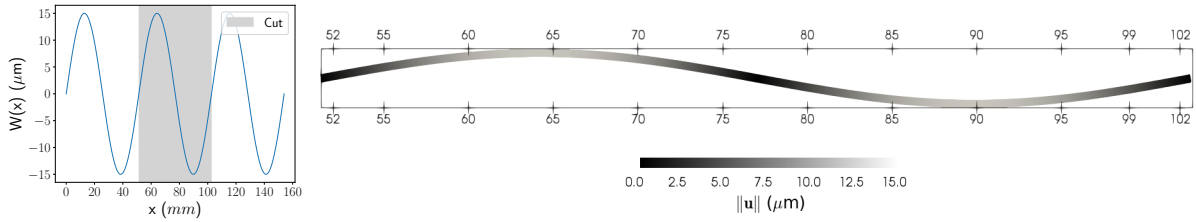

(a) (b)

Figure 5: Considered mode $n = 6$ with $W_0 = 15$ μm applied on the configuration Figure 1: (a) spatial component W and the simulated "cut" zone; and (b) aluminium substrate warped by $1000 \times \boldsymbol{u}$ and colored by $\|\boldsymbol{u}\|$.

Eq. (33) is used to relate the normal stiffness k to the classic adhesive strength σ_c^{adh}. Cancellation of the derivative $\frac{d\sigma}{d[\![u]\!]}$ yields

$$k = \frac{2}{3}\frac{g_c^{adh}}{\omega_c^2} \quad \text{where the critical opening is here} \quad \omega_c = \frac{3}{8}\frac{g_c^{adh}}{\sigma_c^{adh}}. \tag{34}$$

Values $g_c^{adh} = 0.5$ J / m^2 and $\sigma_c^{adh} = 1$ MPa of Tab. 2 imply $k = 9.48 \times 10^{12}$ Pa / m thanks to Eq. (34).

5. Numerical simulations

5.1. Generalities

First of all, sanity checks are performed seperately on a cohesive and adhesive case in order to verify our implementation. They are presented in Appendix E.

Selected mode. The coupled adhesive / brittle failure method described in Section 3 is now applied to the configuration of Figure 1. It is recalled that the load $W(x)$ is a flexural mode given by

$$W(x) = W_0 \sin\left(\frac{n\pi x}{a}\right). \tag{35}$$

The sixth mode of the structure $n = 6$ together with the spatial amplitude $W_0 = 15$ μm are chosen. This mode is displayed in Figure 5 and corresponds to the resonance frequency $f \simeq 8.4$ kHz [22, Tab. 3] ($\omega \simeq 53300$ rad / s). This resonance frequency is high enough to observe fractures while staying below 15 kHz as recommended in Subsection 2.1.

Computational settings. A progressive load is adopted for all tests: the mode amplitude is increased at each iteration until reaching $W_0 = 15$ μm. For computational cost considerations, simulations are performed only on one wave length of the mode thanks to periodic boundary conditions applied on right and left boundaries. The simulated wave length is indicated by the "cut" shaded zone in Figure 5(a). The ice layer (Ω_1) is discretized into 1 208 220 triangular cells of maximum size $h_{max} \simeq 24.8$ μm generated by GMSH [96]. Only the upper part, with respect to the neutral line h_n, of the aluminium substrate (Ω_2) is meshed with 283 386 triangular cells of maximum size $h_{max} \simeq 23.2$ μm. Since there is no bulk damage in aluminium, the lower part is no use to simulate. The crack regularization parameter ℓ is taken to be $\ell = 8 \times h_{max} = 198.4$ μm within the ice layer—corresponding to 40 cells in the crack support [59, Eq. (3.14)]. The fine mesh considered here allows non-diffusive results while taking a relative large amount of cells within the support to ensure a well-resolved crack. Some results are presented with a zoom on the range [57.5 , 71] mm of the simulated wave length—corresponding to the maximum tensile stress region (called an antinode) on the top surface of the ice layer. This region is displayed on Figure 6 representing initial, *i.e.* without crack, tensile σ_{xx} and shear $\sigma_{xy} = \sigma_{yx}$ stresses in the ice layer (Ω_1).

Outline of the section. This section is organized as follows: (i) a full cohesive / adhesive computation with Algorithm 1 and Model 1 (Case 4) is progressively obtained through intermediate tests (Cases 1, 2 and 3) in Subsection 5.2; (ii) the previous full cohesive / adhesive result (Case 4) is detailed and discussed in Subsection 5.3; and (iii) Subsection 5.4 presents a deeper insight into the adhesive modelling by investigating results given by Algorithm 1 with Model 2 (Case 5) and Model 3 (Case 6). All test cases are summarized in Tab. 3 and described in each subsection.

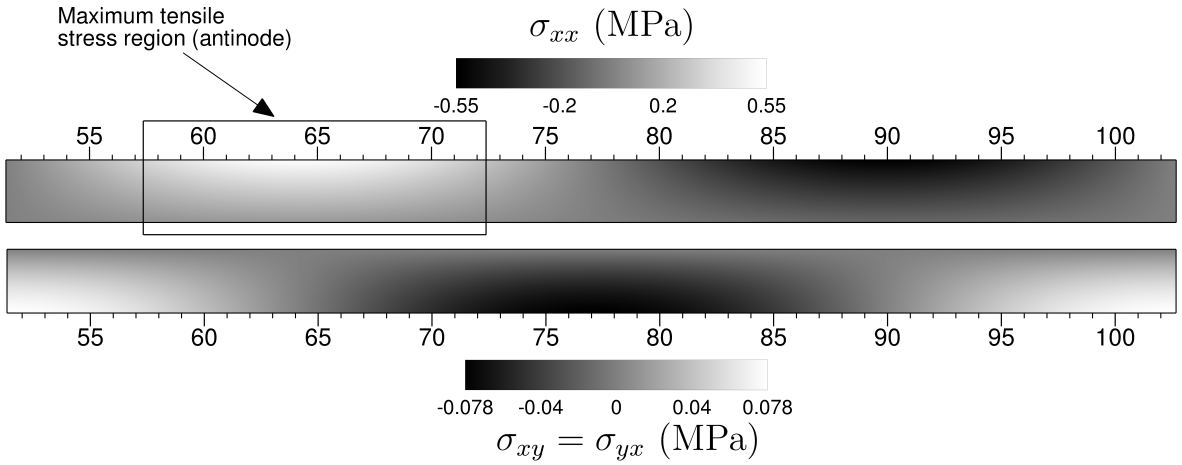

Figure 6: Initial stresses in the ice layer Ω_1: (top) tensile stress σ_{xx}; and (bottom) shear stress $\sigma_{xy} = \sigma_{yx}$.

Case Subsection	Cohesive/Adhesive	Substrate	Adhesive Model
Case 1 Subsection 5.2	Pure cohesive	No	No adhesive model: imposed disp. at the ice bottom boundary
Case 2 Subsection 5.2	Cohesive/Adhesive	Yes	Model 1: imposed zero adhesive damage $\beta = 0$
Case 3 Subsection 5.2	Pure cohesive	Yes	No adhesive model: damageable interface with non-zero thickness Substrate disp. exactly transmitted
Case 4 Subsections 5.2 & 5.3	Cohesive/Adhesive	Yes	Model 1
Case 5 Subsection 5.4	Cohesive/Adhesive	Yes	Model 2
Case 6 Subsection 5.4	Cohesive/Adhesive	Yes	Model 3

Table 3: Test cases performed in Section 5.

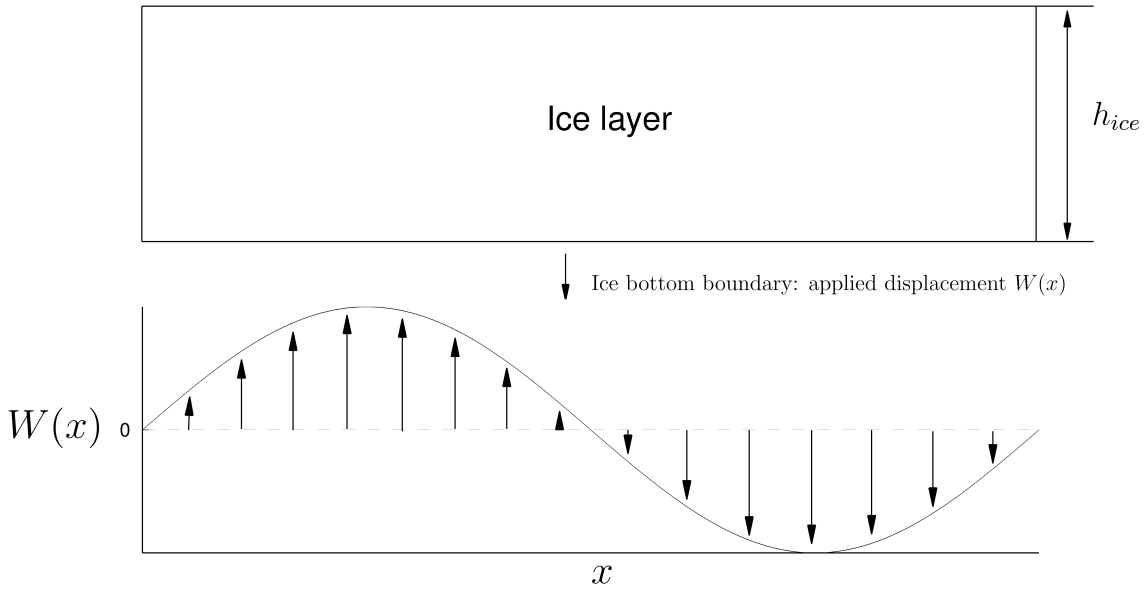

Figure 7: Case 1: domain and boundary condition

5.2. Towards full cohesive / adhesive results step by step

We start with intermediate results—Cases 1, 2 and 3—going progressively to a full cohesive / adhesive computation obtained with Algorithm 1—Case 4. These results consist in comparisons between pure cohesive—model assessed and discussed several times on other fracture problems [59, and references therein]—and cohesive / adhesive cases. It gives us more confidence in the adhesive modelling while providing a deeper understanding on the fracture behavior predicted by the model.

Case 1 (pure cohesive). In this simplified test, only the ice layer is simulated. To mimick the presence of the aluminium substrate which undergoes the flexural mode on its neutral line, displacements are imposed on the adhesive interface—bottom boundary of the ice layer equivalently. These displacements are extracted after a purely elastic computation: initialization of Algorithm 1. Domain and boundary condition are shown in Figure 7. The crack behavior is displayed in Figure 9 (left). The crack nucleates on the first antinode where the tensile stress is maximum. Note that the elastic energy spliting (7) forbids the degradation of its compressive part and, consequently, crack nucleation in compression (second antinode). It then propagates through the entire ice thickness. Once reaching the ice bottom boundary, the fracture branches and the crack continues its propagation along the bottom boundary.

Case 2 (cohesive / adhesive). In Case 2, the substrate is now added so that the displacements are applied on the neutral line : see Figure 8. The adhesive interface is modelled with Model 1 but $\beta = 0$ is imposed. Case 2 thus corresponds to a full coupled adhesive / brittle failure result in which the adhesive damage is set to zero throughout the entire calculation. To that end, the computation is done with Algorithm 1 and Model 1 but: (i) updates of the history field $\mathcal{H}^i_\beta$ in (30) and the adhesive damage β^i in (31) are removed; and (ii) $\beta^i = 0$ is taken in (32). On Figure 9 (right), Case 2 shows a very similar crack behavior as compared to Case 1. In particular, the crack nucleates at the same position (on the first antinode of the wave length) and follows the same path. Adhesive boundary conditions in (32) correctly transfer efforts from the substrate to the ice when the adhesive interface is undamaged, *i.e.* when $\beta = 0$. One can observe however a small difference as the crack branches a little earlier for Case 1.

Case 3 (pure cohesive). Case 3 is presented in Figure 10. Now, the adhesive damage is authorized to grow but Case 3 models the adhesive interface as a damageable homogeneous isotropic elastic layer of non-zero thickness h_{layer}. The ice and the adhesive layers are hence discretized with a common mesh. There is no interface between the ice and

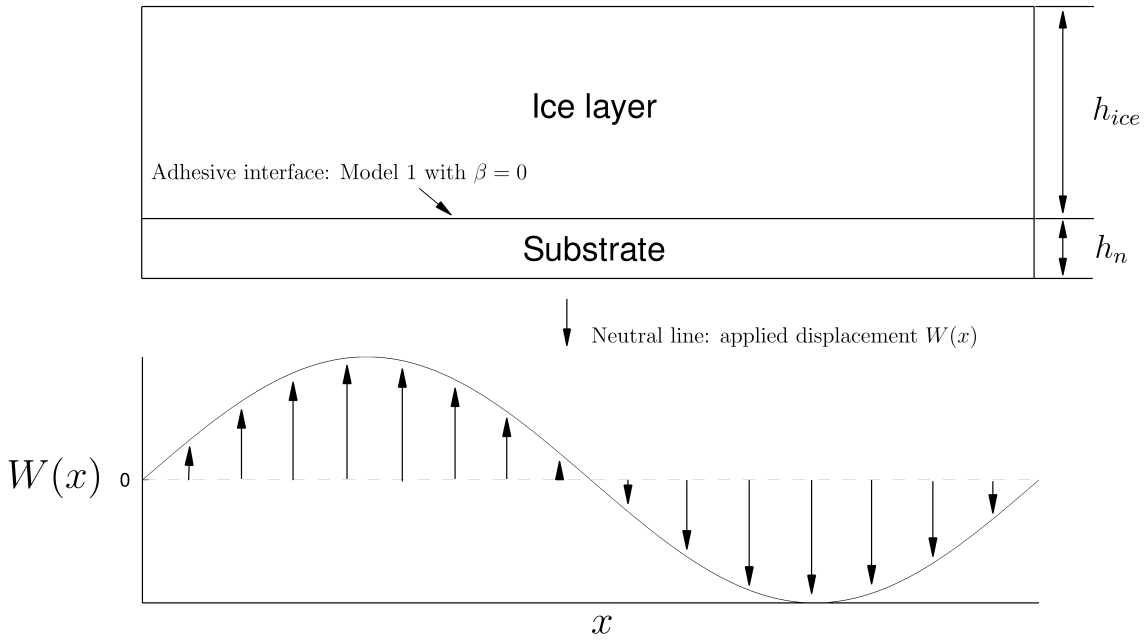

Figure 8: Case 2: domain and boundary condition

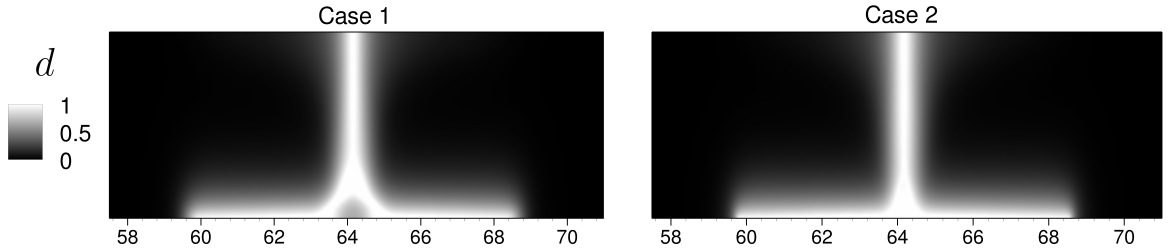

Figure 9: Final damage fields: (left) Case 1; and (right) Case 2. Zoom around the maximum tensile stress region (antinode) displayed in Figure 6.

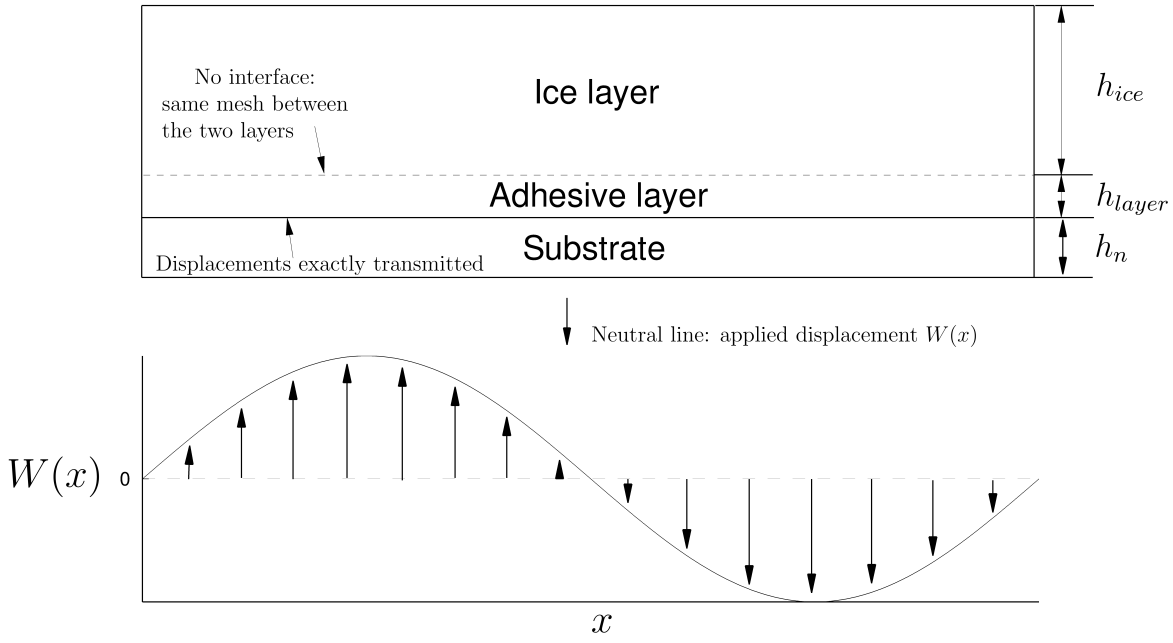

Figure 10: Case 3: domain and boundary condition

the adhesive layer and the adhesive damage is here given by the brittle fracture model of Subsection 3.1—such as the cohesive fracture in the ice. According to Subsection 3.1, the adhesive layer is characterized by a Young's modulus c_{layer}, a Poisson's ratio ν_{layer}, a critical energy release rate g_c^{layer} and a critical strength σ_c^{layer}. The Young's modulus c_{layer} is related to the normal stiffness k computed in Section 4 while the others paramaters are

$$c_{layer} = k\, h_{layer}, \quad \nu_{layer} = 0.3, \quad g_c^{layer} = g_c^{adh}, \quad \text{and} \quad \sigma_c^{layer} = \sigma_c^{adh},$$

where g_c^{adh} and σ_c^{adh} are given in Tab. 2. The interface thickness is $h_{layer} = h_{ice} / 10 = 0.2$ mm. Of course, the value of the adhesive thickness h_{layer} plays an important role in the comparison: one has to consider an adhesive layer as thin as possible in Case 3 to be comparable with Case 4. In practice, h_{layer} is limited by the number of cells. The layer has to be discretized by a sufficient number of cells so as to correctly resolved the cohesive crack inside: a vanishing layer thickness implies a dramatic increase of the computational cost. The result is given in Figure 12 (top): the crack nucleates on the first antinode, propagates through the ice thickness and finally causes damage into the adhesive layer, *i.e.* delamination.

Case 4 (cohesive / adhesive). Case 4 is very similar to Case 3 but the adhesive interface in now of zero-thickness. The adhesive damage β is computed thanks to Model 1 described in 3.2. This case corresponds to the full cohesive / adhesive Algorithm 1 (with Model 1): see Figure 11. Figure 12 shows a very good agreement between Cases 3 and 4.

5.3. A closer look to the predicted ice shedding mechanism

This subsection goes into further details concerning Case 4. It is recalled that the computation is done here with Algorithm 1 where the adhesive modelling is given by Model 1: see Figure 11 for the domain and boundary condition. The goal is to take a closer look on the ice shedding mechanism at play. Figure 13 shows some intermediate iterations during the convergence process of Algorithm 1. Again, the failure process begins with a cohesive fracture on the first antinode of the wave length: Figure 13 (top left) and (top right). When the cohesive fracture almost crosses the ice through its entire thickness, the stress redistribution provides enough energy stored in microscopic bonds to initiate adhesive damage: Figure 13 (middle left) and (middle right). Then the adhesive damage spreads: Figure 13 (bottom left) and (bottom right). The model thus predicts a delamination caused by a cohesive fracture initating at the top of the ice layer on the first antinode of the wave length. *This supports mechanism 1 introduced in [22].*

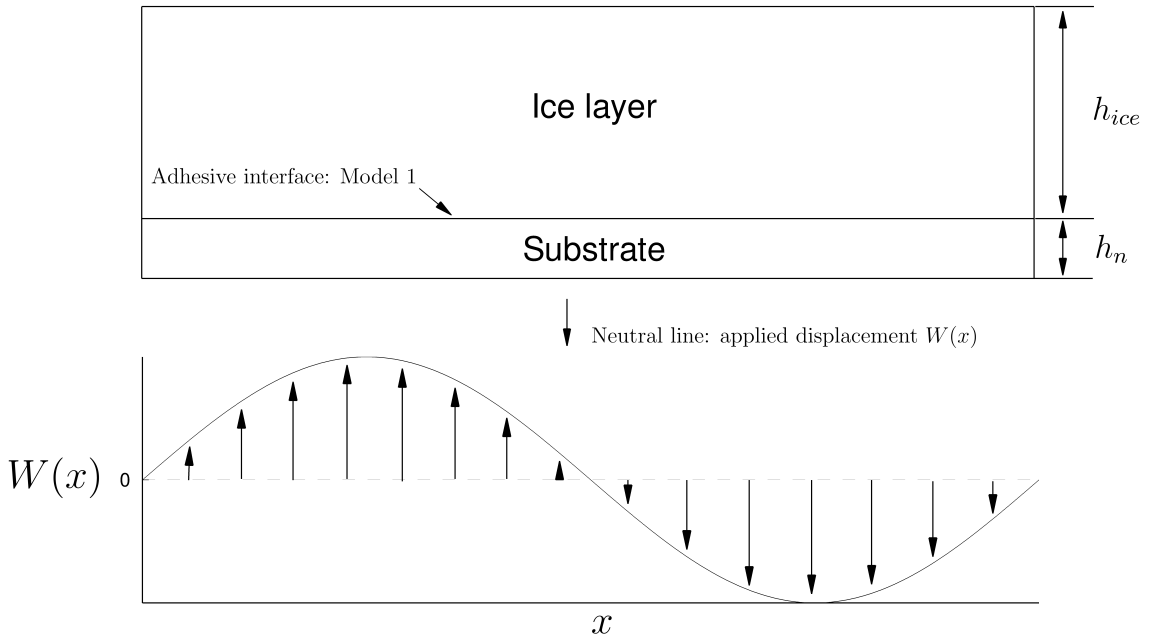

Figure 11: Case 4: domain and boundary condition

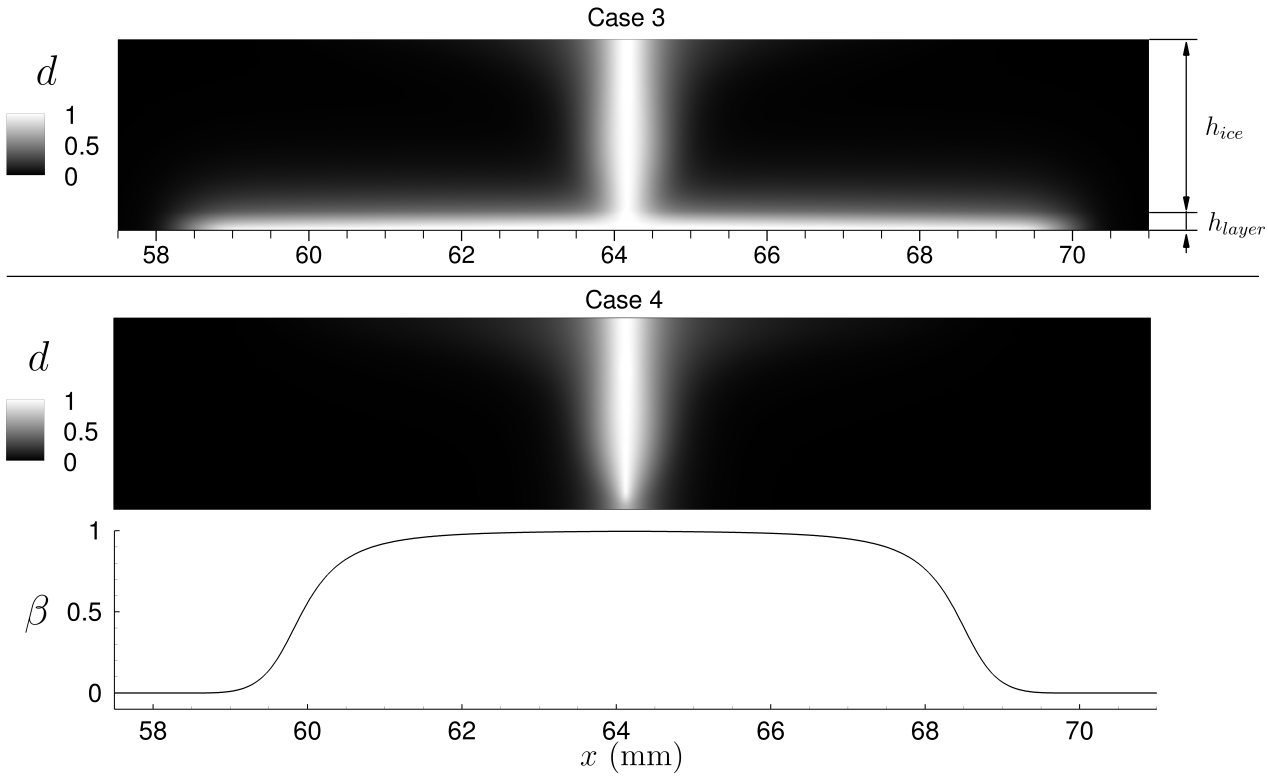

Figure 12: Final damage fields: (top) Case 3; and (bottom) Case 4. Zoom around the maximum tensile stress region (antinode) displayed in Figure 6.

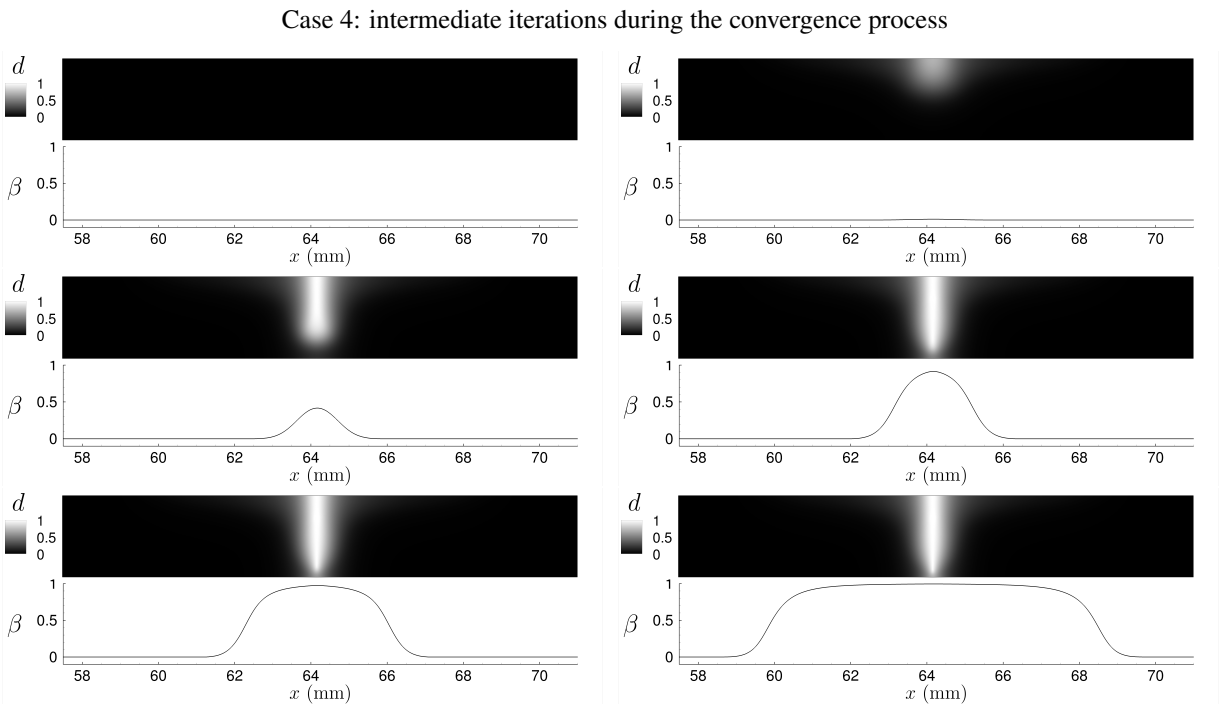

Figure 13: Case 4. Final damage fields: (top left) iteration 0; (top right) iteration 75; (middle left) iteration 80; (middle right) iteration 85; (bottom left) iteration 90; (bottom right) final iteration 148. Zoom around the maximum tensile stress region (antinode) displayed in Figure 6.

5.4. Going further into the adhesive modelling

This last subsection is dedicated to the two more elaborated adhesive models—Case 5 (Model 2) and Case 6 (Model 3). Since the consideration of a pure Mode I failure is questionable as stated in Section 3.2, the effect of the introduction of Mode II failure is investigated through numerical experiments in this part.

Case 5 (Model 2). Case 5 corresponds to a cohesive / adhesive computation by Algorithm 1 on the configuration of Figure 11 but with adhesive Model 2. It is recalled that the stored energy in microscopic bonds associated with tangential displacements $[\![\boldsymbol{u}]\!]_\tau$—parametrized by the coefficient $\alpha_\tau = \frac{k_\tau}{k}$—can now be degraded into crack surface energy. As explained in Subsection 3.2, the tangential stiffness k_τ presents some difficulties to calibrate without introducing additional hypotheses. A fit with experimental dis explicitely mentioned to beata is also excluded as we do not want to influence ice shedding trends. A sensitivity study on α_τ is thus performed. It should be noted that $\alpha_\tau = 0.25$ corresponds to the stiffness ratio of an homogeneous isotropic elastic layer of vanishing thickness $h_{layer} \to 0$ [97, and references therein]

$$\alpha_\tau = \frac{k_\tau}{k} = \frac{1-2\,\nu_{layer}}{2(1-\nu_{layer})} \tag{36}$$

where ν_{layer} is taken as in Subsection 5.2, *i.e.* $\nu_{layer} = 0.3$. Damages d and β are displayed on the whole simulated wave length in Figure 14 for $\alpha_\tau = 0.1$ and $\alpha_\tau = 1$. Figure 16 (left) presents the adhesive damage β for $0.1 \leq \alpha_\tau \leq 1$. The case $\alpha_\tau < 0.1$ yields no cohesive or adhesive damage while $\alpha_\tau > 1$ gives very similar results compared to $\alpha_\tau = 1$. The choice $\alpha_\tau < 0.1$ implies a stiffness k_τ too low for transfering enough efforts from the substrate to the ice and consequently does not allow damage to initiate. Interesting results are obtained for $0.1 \leq \alpha_\tau \leq 1$ and particularly for $\alpha_\tau = 0.1$. *Mechanism 1 [22] is observed for* $\alpha_\tau \geq 0.25$. However *the value* $\alpha_\tau = 0.1$ *clearly highlights a mechanism close to mechanism 2* [22]: direct delamination is initiated at nodes (maximum shear stress) without cohesive fracture. More precisely, the adhesive interface is not fully debonded since $\beta \simeq 0.8$ and does not reach 1. At this stage, the model predicts the two ice shedding mechanisms postulated in [22] depending on the value of the tangential stiffness k_τ—or $\alpha_\tau = \frac{k_\tau}{k}$ equivalently.

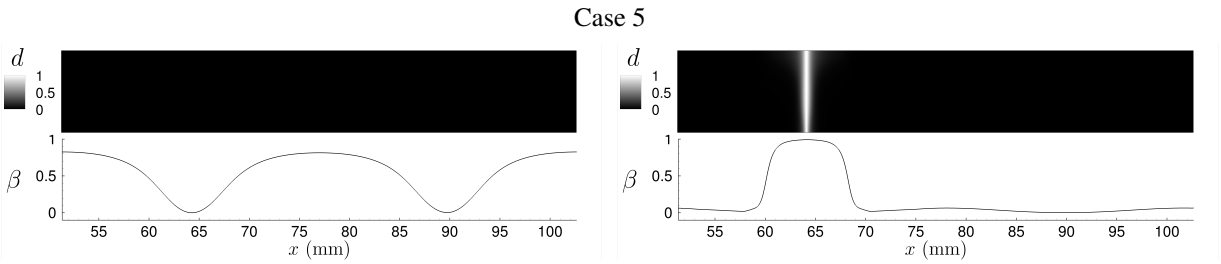

Figure 14: Case 5. Final damage fields: (left) $\alpha_\tau = 0.1$; and (right) $\alpha_\tau = 1$.

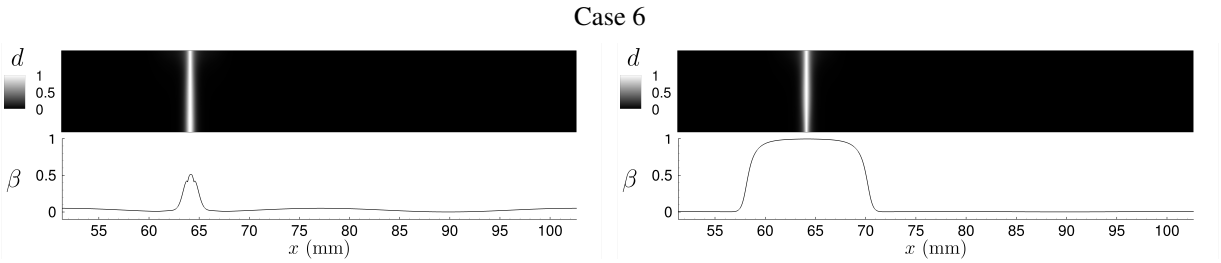

Figure 15: Case 6. Final damage fields: (left) $\alpha_\tau = 0.05$; and (right) $\alpha_\tau = 0.75$.

Case 6 (Model 3). In Case 6, the adhesive modelling incorporates anisotropy in the adhesive fracture energy ϕ_{adh}: computation with Algorithm 1 on the configuration Figure 11 with adhesive Model 3. The anisotropy takes the form of two different critical energy release rates g_c^{adh} for Mode I and $g_c^{adh,II}$ for Mode II. It is recalled that $g_c^{adh} = 0.5\,\mathrm{J/m^2}$ and $g_c^{adh,II} = 10\,g_c^{adh} = 5\,\mathrm{J/m^2}$. Figures 15 and 16 (right) respectively display cohesive damage d and adhesive damage β for some interesting values $0.05 \leq \alpha_\tau \leq 0.75$. As for Case 5, $\alpha_\tau < 0.05$ leads to a too low tangential stiffness k_τ for correctly transfering efforts. Consequently, no damage appears for $\alpha_\tau < 0.05$, neither cohesive nor adhesive. Unlike Case 5 however, $\alpha_\tau \geq 1$ puts forward the limitation of the method and gives too diffusive results to be interpreted. A possible solution could be the use of a finer mesh but this is beyond the scope of this paper. A more interesting result is that *only mechanism 1 [22] is now observed*: a cohesive fracture initiates on the first antinode of the wave length, then propagates through the entire thickness and causes delamination. Full delamination—*i.e.* $\beta = 1$—begins with the value $\alpha_\tau = 0.25$, for which a close result compared to Case 5—excluding $\alpha_\tau = 0.1$—is obtained. Excluding $\alpha_\tau = 0.1$ again, inspection of Figure 16 shows that the two values of $g_c^{adh,II}$ yields the same fracture mechanism at fixed α_τ.

As a conclusion to this section, *one may note that, generally, all our numerical experiments give more weight to mechanism 1 introduced by Budinger et al. [22].*

6. Conclusion

This paper deals with a phase-field variational approach for fracture applied to electromechanical de-icing. While the obtained method is limited either by its phase-field component (fine meshes required) or by ice applications (uncertainties due to identification of needed paramaters), it provides a useful framework to study fracture propagation and ice shedding in this context. Numerical experiments are conducted to highlight ice shedding trends and compare them with the postulated mechanisms of Budinger *et al.* [22].

The full derivation of the adhesive / brittle failure model is presented. Modelling choices and parameters involved in the model are discussed and justified. Several test cases are performed on the pure flexural mode $n = 6$ corresponding to a frequency around 8.4 kHz. First, full cohesive / adhesive results are obtained step by step through comparisons with pure cohesive cases. Then, the three proposed adhesive models are investigated. Model 1 only considers Mode I failure. Models 2 and 3 improve the adhesive modelling by gradually introducing Mode II failure. Whatever the model used—with the exception of Model 2 with $\alpha_\tau = 0.1$—*mechanism 1 [22] is observed.*

In a close future, ongoing work includes direct applications of the method: different modes staying in a reasonable frequency range (a few kHz) with different configurations will be tested. In particular, these additional test cases could

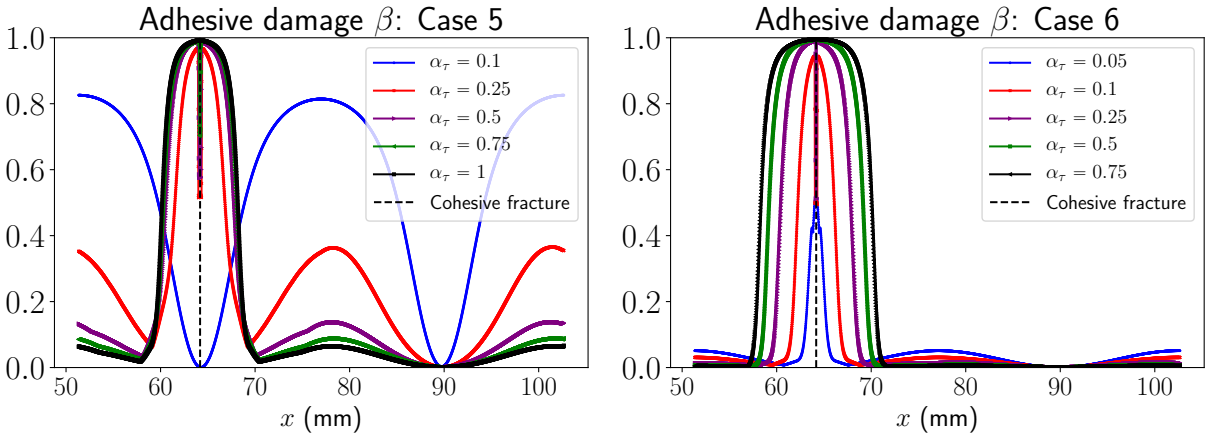

Figure 16: Adhesive damage β for different values of α_τ: (left) Case 5 with α_τ ranges from 0.1 to 1; (right) Case 6 with α_τ ranges from 0.05 to 0.75.

be used to assess the other conclusions drawn by Budinger *et al.* [22] such as the effect of thicker ice layers or the efficiency of mixed extensional/flexural modes. The phase-field variational method will also be confronted to reduced models for optimization purposes. Parametric and/or topological optimization will be performed with the help of selected reduced models for designing more efficient electromechanical systems. From a numerical point of view, the method can be improved in many ways. Concerning the model, dynamic effects or the coupling between adhesive and cohesive damages and its possible improvements would be worth investigating. Finally, parallelization, three-dimensional geometry would be valuable additions to get a closer look at ice shedding mechanisms in the context of electromechanical de-icing systems.

Acknowledgment

This work is funded by the STAE foundation through the ReMOVEICE project.

Appendix A. Boundedness of the bulk damage variable d

The methodology of [98] is followed. The weak formulation

$$\int_\Omega a\,u\,v\,dV + \int_\Omega b\,\boldsymbol{\nabla} u\cdot\boldsymbol{\nabla} v\,dV = \int_\Omega f\,v\,dV, \tag{A.1}$$

is considered, where a, b, f are positive and v is a test function. For the above fomulation, a maximum principle holds on u:

$$u \geq \inf_\Omega f. \tag{A.2}$$

Now, the weak formulation of (28) is

$$\int_{\Omega_1} \left[2\,(1-\xi)\,\tfrac{g_c}{c_0\,\ell} + K\,\mathcal{H}_d\right] d\,v\,dV + \int_{\Omega_1} \tfrac{g_c\,\ell}{c_0}\boldsymbol{\nabla} d\cdot\boldsymbol{\nabla} v\,dV = \int_{\Omega_1} \left[K\,\mathcal{H}_d - \tfrac{g_c}{c_0\,\ell}\xi\right] v\,dV, \tag{A.3}$$

after the linearization $f_1(d) = K\,(d-1)$ and the introduction of the history function $\mathcal{H}_d$. Consequently, the result (A.2) applies if

$$\left[K\,\mathcal{H}_d - \tfrac{g_c}{c_0\,\ell}\xi\right] \geq 0 \text{ and } \left[2\,(1-\xi)\,\tfrac{g_c}{c_0\,\ell} + K\,\mathcal{H}_d\right] \geq 0 \tag{A.4}$$

and we get

$$d \geq \inf_\Omega \left[K\,\mathcal{H}_d - \tfrac{g_c}{c_0\,\ell}\xi\right] \Rightarrow d \geq 0. \tag{A.5}$$

As $\mathcal{H}_d \geq 0$, $K \geq 0$ and $\frac{g_c}{c_0\,\ell} \geq 0$, the second part of (A.4) is fullfilled with $\xi = 0.5$. The first part of (A.4) justifies the modification of the source term in Eq. (28), yielding Eq. (29). Note that a similar analysis with $d^\star = 1 - d$ leads to $d^\star \geq 0$, hence $d \leq 1$.

Appendix B. Computation the two parameters a_2 and a_3 in the brittle failure model

The equivalent Cohesive Zone Model of the model described in Subsection 3.1 is given by Wu in [59, Eqs. (3.4a) and (3.4b)]

$$\sigma(d^\star) = \sigma_c \sqrt{\frac{[\xi + (1-\xi)\,d^\star]\,(1-d^\star)^p}{\xi\,P(d^\star)}}, \tag{B.1}$$

$$\omega(d^\star) = \frac{4\,g_c\,\sqrt{\xi}}{c_0\,\sigma_c} \int_0^{d^\star} \left[\frac{P(d^\star)}{(1-d^\star)^p}\,\frac{\xi + (1-\xi)\beta}{\xi + (1-\xi)\,d^\star} - \frac{P(\beta)}{(1-\beta)^p}\right]^{-1/2} \frac{\sqrt{\beta}P(\beta)}{(1-\beta)^p} d\beta, \tag{B.2}$$

parametrized by the maximum damage $d^\star$. These relations are computed in the one-dimensional case where the stress σ is homogeneous (no body forces). Note that the critical stress σ_c in this framework is

$$\sigma_c = \sqrt{\frac{2\,c_{ice}\,g_c}{c_0\,\ell}\,\frac{\xi}{a_1}}, \tag{B.3}$$

justifying the expression of a_1 in Eq. (10). The polynomial P is introduced in the geometric function α in Eq. (8). For the Cohesive Zone Model (B.1)-(B.2), it is possible to compute its initial slope k_0 and ultimate crack opening ω_c [59, Eqs. (3.7) and (3.8b)]

$$k_0 = -\frac{c_0}{4\,\pi}\,\frac{\sigma_c^2}{g_c}\,\frac{\left[\xi(a_2+p+1)-1\right]^{3/2}}{\xi^2}, \tag{B.4}$$

$$\omega_c = \begin{cases} 0 & \text{for } p < 2 \\ \frac{2\,\pi\,g_c}{c_0\,\sigma_c}\sqrt{\xi\,P(1)} & \text{for } p = 2 \\ +\infty & \text{for } p > 2. \end{cases} \tag{B.5}$$

From Eqs. (B.4) and (B.5), parameters a_2 and a_3 are deduced

$$a_2 = \frac{1}{\xi}\left[\left(-\frac{4\,\pi\,\xi^2}{c_0}\,\frac{g_c}{\sigma_c^2}\,k_0\right)^{2/3} + 1\right] - (p+1) \quad \text{and} \quad a_3 = \begin{cases} 0 & \text{for } p > 2 \\ \frac{1}{a_2}\left[\frac{1}{\xi}\left(\frac{c_0\,\omega_c\,\sigma_c}{2\,\pi\,g_c}\right)^2 - (1+a_2)\right] & \text{for } p = 2 \end{cases} \tag{B.6}$$

Once the classical softening law is targeted—mainly influenced by the parameter p—the initial slope k_0 and the ultimate crack opening ω_c are fixed thus determining a_2 and a_3 through (B.6). In this paper, the choice $p = 2$ allows targeting a linear softening law [59, Eqs. (3.9) and (3.20)]

$$k_0 = -\frac{\sigma_c^2}{2\,g_c} \tag{B.7}$$

$$\omega_c = \frac{2\,g_c}{\sigma_c} \tag{B.8}$$

as depicted in Figure B.17.

Appendix C. Computation of the adhesive boundary conditions

Adhesive boundary conditions on Γ_2 in (16) become

$$\boldsymbol{R}_1 = -\left(\frac{\partial\gamma}{\partial\boldsymbol{u}_1} + \frac{\partial\phi_{adh}}{\partial\boldsymbol{u}_1}\right) = -F\left(\beta\,,\,[\![\boldsymbol{u}]\!]\right)\cdot[\![\boldsymbol{u}]\!] \tag{C.1}$$

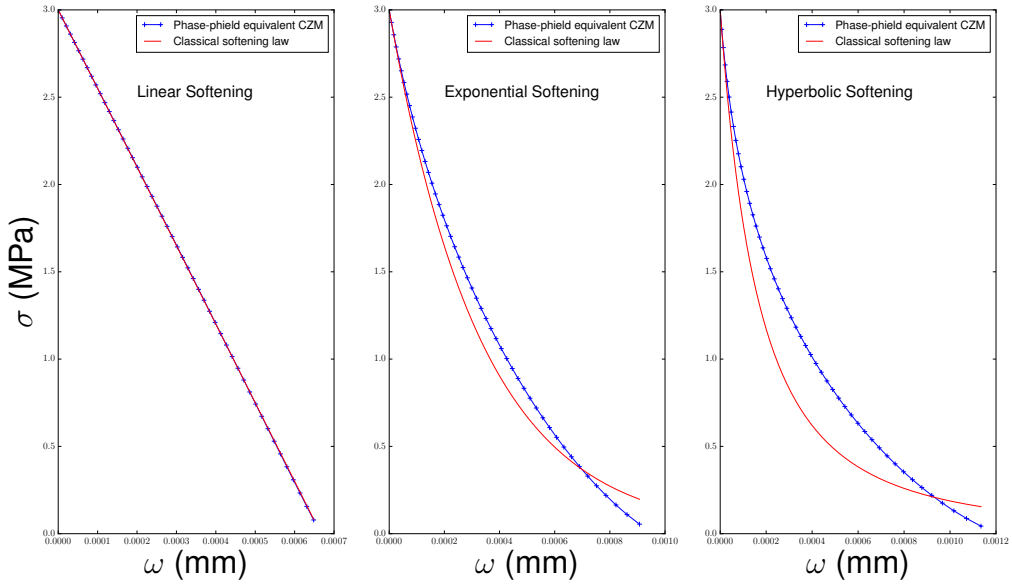

Figure B.17: Equivalent Cohesive Zone Model (CZM) (B.1)-(B.2) compared to three classical softening laws for $\xi = 0.5$, $p = 2$, $g_c = 1$ J / m^2 and $\sigma_c = 3$ MPa. Coefficients a_2 and a_3 are computed with (B.6) where the initial slope k_0 and ultimate crack opening ω_c correspond to the targeted softening law.

where $F(\beta, [\![\boldsymbol{u}]\!])$ is

$$F(\beta, [\![\boldsymbol{u}]\!]) = k\, f_2(\beta)\left[\delta_+ \begin{pmatrix} sin^2(\theta) & -sin(\theta)\,cos(\theta) \\ -sin(\theta)\,cos(\theta) & cos^2(\theta) \end{pmatrix} + \alpha_\tau \begin{pmatrix} cos^2(\theta) & sin(\theta)\,cos(\theta) \\ sin(\theta)\,cos(\theta) & sin^2(\theta) \end{pmatrix}\right] + k_\infty\, \delta_- \begin{pmatrix} sin^2(\theta) & -sin(\theta)\,cos(\theta) \\ -sin(\theta)\,cos(\theta) & cos^2(\theta) \end{pmatrix} + \underbrace{k \left(\frac{1}{(g_c^{adh})^{II}} - \frac{1}{(g_c^{adh})^{I}}\right)\left(\frac{g_c^{adh}}{\gamma_\beta}\beta\right)^2 \left[\delta_+ \gamma_\beta^{II} \begin{pmatrix} sin^2(\theta) & -sin(\theta)\,cos(\theta) \\ -sin(\theta)\,cos(\theta) & cos^2(\theta) \end{pmatrix} + \alpha_\tau\, \gamma_\beta^{I} \begin{pmatrix} cos^2(\theta) & sin(\theta)\,cos(\theta) \\ sin(\theta)\,cos(\theta) & sin^2(\theta) \end{pmatrix}\right]}_{\frac{\partial \phi_{adh}}{\partial \boldsymbol{u}_1}}, \quad \text{(C.2)}$$

with

$$\delta_+ = \begin{cases} 0 & \text{if} \quad [\![\boldsymbol{u}]\!]_n < 0 \\ 1 & \text{if} \quad [\![\boldsymbol{u}]\!]_n \geq 0 \end{cases},$$

$\delta_- = 1 - \delta_+$ and θ defined in Figure C.18. For adhesive Models 1 and 2, the term $\frac{\partial \phi_{adh}}{\partial \boldsymbol{u}_1}$ cancels in Eqs (C.1) and (C.2) since $\phi_{adh}(\beta, \boldsymbol{u}_1, \boldsymbol{u}_2) = \phi_{adh}(\beta)$. Finally, the force $\boldsymbol{R}_2$ is directly deduced by

$$\boldsymbol{R}_2 = -\frac{\partial(\gamma+\phi_{adh})}{\partial \boldsymbol{u}_2} = -\frac{\partial(\gamma+\phi_{adh})}{\partial [\![\boldsymbol{u}]\!]}\frac{\partial [\![\boldsymbol{u}]\!]}{\partial \boldsymbol{u}_2} = \frac{\partial(\gamma+\phi_{adh})}{\partial [\![\boldsymbol{u}]\!]}\frac{\partial [\![\boldsymbol{u}]\!]}{\partial \boldsymbol{u}_1} = \frac{\partial(\gamma+\phi_{adh})}{\partial \boldsymbol{u}_1} = -\boldsymbol{R}_1, \quad \text{(C.3)}$$

ensuring that $\boldsymbol{\sigma}_1 \cdot \boldsymbol{n}_1 = -\boldsymbol{\sigma}_2 \cdot \boldsymbol{n}_2$ regarding the two adhesive boundary conditions in (16). The stress tensor is thus continuous along the normal direction through the adhesive interface whatever the adhesive model.

Appendix D. Derivation of the full coupled adhesive / brittle failure model

This appendix is dedicated to the brief derivation of the full coupled adhesive / brittle failure model of SubSection 3.3. It is important to recall that the configuration Figure 4 is completed with Dirichlet and Neumann boundary

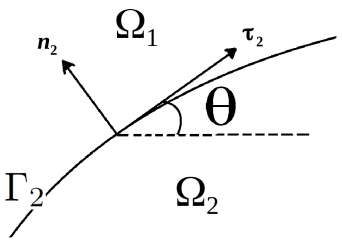

Figure C.18: Definition of the angle θ.

conditions both in Ω_1 and Ω_2 for generality and that Ω_1 can undergo brittle failures while no bulk damage is considered in Ω_2. Notations introduced in SubSection 3.3 are: for $i = 1, 2$, $\partial\Omega_i$ is decomposed into $\partial\Omega_i = \Gamma_1^{\Omega_i} \cup \Gamma_2 \cup \Gamma_3^{\Omega_i}$ where $\Gamma_1^{\Omega_i}$ supports Neumann boundary condition $\boldsymbol{\sigma}_i \cdot \boldsymbol{n}_i = \boldsymbol{f}_{surf}$, $\Gamma_3^{\Omega_i}$ supports Dirichlet boundary condition $\boldsymbol{u}_i = \boldsymbol{u}_d$ and Γ_2 is the common adhesive interface. The total energy of the system is given by Eq. (25)

$$E_{tot} = \underbrace{\int_{\Omega_1} \psi_1(\boldsymbol{\epsilon}_1\,,\, d)\, dV}_{E_{el}^{\Omega_1}} + \underbrace{\int_{\Omega_1} \phi(d\,,\, \boldsymbol{\nabla} d)\, dV}_{E_{crack}} + \underbrace{\int_{\Omega_2} \psi_2(\boldsymbol{\epsilon}_2)\, dV}_{E_{el}^{\Omega_2}} + \underbrace{\int_{\Gamma_2} \phi_{adh}(\beta\,,\, \boldsymbol{u}_1\,,\, \boldsymbol{u}_2)\, d\Gamma}_{E_{adh}} + \underbrace{\int_{\Gamma_2} \gamma(\beta\,,\, \boldsymbol{u}_1\,,\, \boldsymbol{u}_2)\, d\Gamma}_{E_{micro}},$$

and its variation is deduced

$$\begin{aligned}\delta E_{tot} = &\underbrace{\int_{\Omega_1} \left[\frac{\partial \psi_1}{\partial \boldsymbol{\epsilon}_1} : \delta\boldsymbol{\epsilon}_1 + \frac{\partial \psi_1}{\partial d}\, \delta d\right] dV}_{\delta E_{el}^{\Omega_1}} + \underbrace{\int_{\Omega_1} \left[\frac{\partial \phi}{\partial d}\, \delta d + \frac{\partial \phi}{\partial \boldsymbol{\nabla} d} \cdot \delta\boldsymbol{\nabla} d\right] dV}_{\delta E_{crack}} + \underbrace{\int_{\Omega_2} \frac{\partial \psi_2}{\partial \boldsymbol{\epsilon}_2} : \delta\boldsymbol{\epsilon}_2\, dV}_{\delta E_{el}^{\Omega_2}} \\ &+ \underbrace{\int_{\Gamma_2} \left[\frac{\partial \phi_{adh}}{\partial \beta}\delta\beta + \frac{\partial \phi_{adh}}{\partial \boldsymbol{u}_1} \cdot \delta\boldsymbol{u}_1 + \frac{\partial \phi_{adh}}{\partial \boldsymbol{u}_2} \cdot \delta\boldsymbol{u}_2\right] d\Gamma}_{\delta E_{adh}} + \underbrace{\int_{\Gamma_2} \left[\frac{\partial \gamma}{\partial \beta}\delta\beta + \frac{\partial \gamma}{\partial \boldsymbol{u}_1} \cdot \delta\boldsymbol{u}_1 + \frac{\partial \gamma}{\partial \boldsymbol{u}_2} \cdot \delta\boldsymbol{u}_2\right] d\Gamma}_{\delta E_{micro}}. \quad \text{(D.1)}\end{aligned}$$

The total work of external forces is still expressed as Eq. (15)

$$\begin{aligned}W_{ext} = &\underbrace{\int_{\Omega_1} \boldsymbol{f}_{vol} \cdot \delta\boldsymbol{u}_1\, dV + \int_{\partial\Omega_1} \boldsymbol{f}_{surf} \cdot \delta\boldsymbol{u}_1\, d\Gamma}_{\text{External forces acting on } \Omega_1} + \underbrace{\int_{\Omega_2} \boldsymbol{f}_{vol} \cdot \delta\boldsymbol{u}_2\, dV + \int_{\partial\Omega_2} \boldsymbol{f}_{surf} \cdot \delta\boldsymbol{u}_2\, d\Gamma}_{\text{External forces acting on } \Omega_2} \\ &+ \underbrace{\int_{\Gamma_2} (-\boldsymbol{R}_1) \cdot \delta\boldsymbol{u}_1\, d\Gamma + \int_{\Gamma_2} (-\boldsymbol{R}_2) \cdot \delta\boldsymbol{u}_2\, d\Gamma}_{\text{External forces acting on } \Gamma_2}.\end{aligned}$$

Now, the energy conservation principle $\delta E_{tot} = W_{ext}$ yields

$$\begin{aligned}&\int_{\Omega_1} \left[div\,(\boldsymbol{\sigma}_1) + \boldsymbol{f}_{vol}\right] \cdot \delta\boldsymbol{u}_1\, dV + \int_{\Omega_2} \left[div\,(\boldsymbol{\sigma}_2) + \boldsymbol{f}_{vol}\right] \cdot \delta\boldsymbol{u}_2\, dV \\ &\qquad \int_{\Omega_1} \left[\frac{g_c}{c_0\,\ell}\, \alpha'(d) - 2\, \frac{g_c\, \ell}{c_0}\, \Delta d + \frac{\partial \psi_1}{\partial d}\right] \delta d\, dV + \int_{\partial\Omega_1} \left[\frac{g_c\, \ell}{c_0} \boldsymbol{\nabla} d \cdot \boldsymbol{n}_1\right] \delta d\, d\Gamma \\ &+ \int_{\Gamma_2} \left[\frac{\partial \phi_{adh}}{\partial \beta} + \frac{\partial \gamma}{\partial \beta}\right] \delta\beta\, d\Gamma + \int_{\Gamma_2} \left[\frac{\partial \gamma}{\partial \boldsymbol{u}_1} + \frac{\partial \phi_{adh}}{\partial \boldsymbol{u}_1} + \boldsymbol{R}_1\right] \cdot \delta\boldsymbol{u}_1\, d\Gamma + \int_{\Gamma_2} \left[\frac{\partial \gamma}{\partial \boldsymbol{u}_2} + \frac{\partial \phi_{adh}}{\partial \boldsymbol{u}_2} + \boldsymbol{R}_2\right] \cdot \delta\boldsymbol{u}_2\, d\Gamma = 0, \quad \text{(D.2)}\end{aligned}$$

assuming $\boldsymbol{\sigma}_1 = \frac{\partial \psi_1}{\partial \boldsymbol{\epsilon}_1}$ and $\boldsymbol{\sigma}_2 = \frac{\partial \psi_2}{\partial \boldsymbol{\epsilon}_2}$. Eq. (D.2) has to hold for every variation $\delta \boldsymbol{u}_1$, $\delta \boldsymbol{u}_2$, δd, $\delta \beta$, therefore

$$
\begin{array}{lll}
-div(\boldsymbol{\sigma}_1(\boldsymbol{\epsilon}_1\,,\, d)) = \boldsymbol{f}_{vol} & \text{in} & \Omega_1 \\
\boldsymbol{R}_1 = -\left(\frac{\partial \gamma}{\partial \boldsymbol{u}_1} + \frac{\partial \phi_{adh}}{\partial \boldsymbol{u}_1}\right) & \text{on} & \Gamma_2 \\
\frac{g_c}{c_0\,\ell}\,\alpha'(d) - 2\,\frac{g_c\,\ell}{c_0}\,\Delta d = -\frac{\partial \psi_1}{\partial d} & \text{in} & \Omega_1 \\
\boldsymbol{\nabla} d \cdot \boldsymbol{n}_1 = 0 & \text{on} & \partial\Omega_1 \\
\frac{\partial \phi_{adh}}{\partial \beta} = -\frac{\partial \gamma}{\partial \beta} & \text{on} & \Gamma_2 \\
-div(\boldsymbol{\sigma}_2(\boldsymbol{\epsilon}_2)) = \boldsymbol{f}_{vol} & \text{in} & \Omega_2 \\
\boldsymbol{R}_2 = -\left(\frac{\partial \gamma}{\partial \boldsymbol{u}_2} + \frac{\partial \phi_{adh}}{\partial \boldsymbol{u}_2}\right) & \text{on} & \Gamma_2
\end{array}
\tag{D.3}
$$

Dirichlet and Neumann boundary conditions are finally added to (D.3). The relation $\frac{\partial \phi_{adh}}{\partial \beta} = -\frac{\partial \gamma}{\partial \beta}$ is replaced by its equivalent counterpart Eq. (24) and the driving force to the bulk damage is expressed as follows $\frac{\partial \psi_1}{\partial d} = f_1(d)\,\psi_0^+(\boldsymbol{\epsilon}_1)$ to get Eqs (26)

$$
\begin{array}{lll}
-div(\boldsymbol{\sigma}_1(\boldsymbol{\epsilon}_1\,,\, d)) = \boldsymbol{f}_{vol} & \text{in} & \Omega_1 \\
\boldsymbol{\sigma}_1 \cdot \boldsymbol{n}_1 = \boldsymbol{f}_{surf} & \text{on} & \Gamma_1^{\Omega_1} \\
\boldsymbol{u}_1 = \boldsymbol{u}_d & \text{on} & \Gamma_3^{\Omega_1} \\
\boldsymbol{\sigma}_1 \cdot \boldsymbol{n}_1 = \boldsymbol{R}_1 = -\left(\frac{\partial \gamma}{\partial \boldsymbol{u}_1} + \frac{\partial \phi_{adh}}{\partial \boldsymbol{u}_1}\right) & \text{on} & \Gamma_2 \\
\frac{g_c}{c_0\,\ell}\,\alpha'(d) - 2\,\frac{g_c\,\ell}{c_0}\,\Delta d = -f_1'(d)\,\psi_0^+(\boldsymbol{\epsilon}_1) & \text{in} & \Omega_1 \\
\boldsymbol{\nabla} d \cdot \boldsymbol{n}_1 = 0 & \text{on} & \partial\Omega_1 \\
\beta = \frac{\gamma_\beta}{g_c^{adh} + \gamma_\beta} & \text{on} & \Gamma_2 \\
-div(\boldsymbol{\sigma}_2(\boldsymbol{\epsilon}_2)) = \boldsymbol{f}_{vol} & \text{in} & \Omega_2 \\
\boldsymbol{\sigma}_2 \cdot \boldsymbol{n}_2 = \boldsymbol{f}_{surf} & \text{on} & \Gamma_1^{\Omega_2} \\
\boldsymbol{u}_2 = \boldsymbol{u}_d & \text{on} & \Gamma_3^{\Omega_2} \\
\boldsymbol{\sigma}_2 \cdot \boldsymbol{n}_2 = \boldsymbol{R}_2 = -\left(\frac{\partial \gamma}{\partial \boldsymbol{u}_2} + \frac{\partial \phi_{adh}}{\partial \boldsymbol{u}_2}\right) & \text{on} & \Gamma_2
\end{array}
$$

Appendix E. Sanity checks for cohesive and adhesive failure

Cohesive failure. The classical single-edge notched plate test of Miehe *et al.* [51, 52] is considered here to verify our implementation of the cohesive failure model. A straight horizontal notch of length 0.5 mm is introduced at the mid-height of a square plate of length 1 mm, with unit out-of-plane thickness. The bottom boundary of the plate is clamped and the top boundary is progressively sheared until reaching a value of $u^\star = 0.014$ mm. Material parameters are set to: Young's modulus $c = 210$ GPa, Poisson's ratio $\nu = 0.3$, critical energy release rate $g_c = 2700$ J / m^2 and material strength $\sigma_c = 2445.42$ MPa. Remaining parameters are kept unchanged: see Eqs (10) and (11). Computations are performed on a mesh with a cell size $h \simeq 0.001$ mm on the crack path and two length scale values $\ell = 0.025$ mm and $\ell = 0.05$ mm. Figure E.19 shows the predicted crack pattern for the two values of ℓ. The same crack pattern is obtained—the length scale ℓ only influences the crack bandwidth—and a good agreement with literature is found.

Adhesive failure. The adhesive modelling is checked thanks to a one-dimensional adhesive traction test described by the configuration Figure 4. Bulk damage in the ice Ω_1 is deactivated and adhesive Model 1 is considered. In that case, adhesive boundary conditions of Appendix C simplify into Eq. (33) recalled here

$$\sigma\left(\llbracket u \rrbracket\right) = k\,(1-\beta)^2\,\llbracket u \rrbracket.$$

Eq. (33) is nothing but the "so-called" traction-separation law of Cohesive Zone Models [38–40] in this one-dimensional case. Several traction forces have been applied to the configuration of Figure 4. For each of them, the stress σ—both in the ice Ω_1 and aluminium Ω_2—together with the displacement jump $\llbracket u \rrbracket$ at the adhesive interface Γ_2 have been extracted after convergence of the algorithm. Obtained stresses are plotted against displacement jump and compared to Eq. (33) in Figure E.20 where the adhesive interface is discretized into 300 points. Numerical interface stresses in ice σ^{ice} and in aluminium σ^{alu} match the analytic traction-separation law (33). In particular, the following points are checked: (i) numerical peak stresses correspond to the introduced adhesive strength $\sigma_c^{adh} = 1$

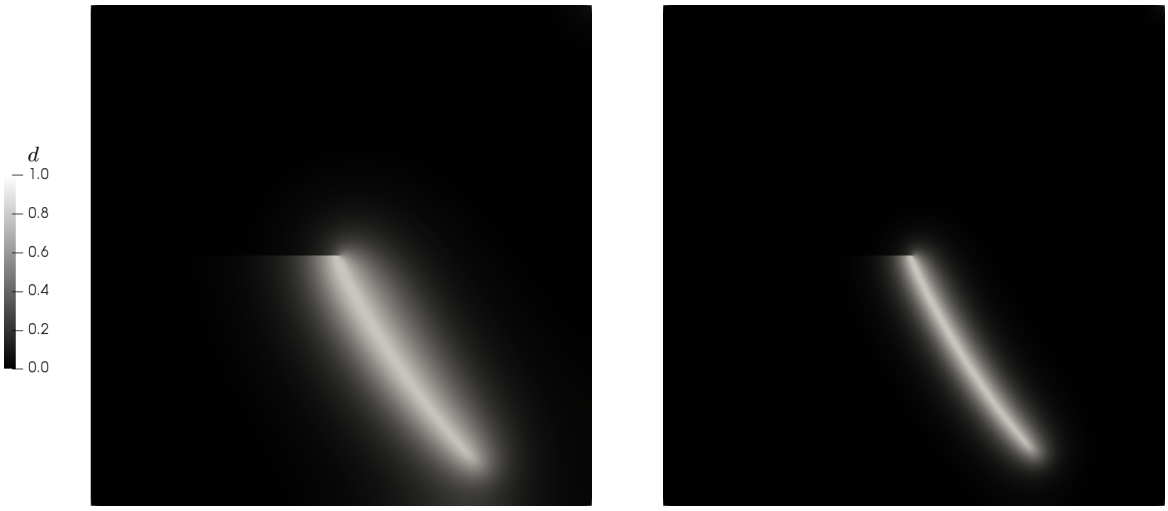

Figure E.19: Single-edge notched plate shear test of Miehe *et al.* [51, 52]: (left) $\ell = 0.05$ mm and (right) $\ell = 0.025$ mm.

MPa of Tab. 2; (ii) the continuity of the stress tensor along the normal direction through the adhesive interface, *i.e.* $\sigma^{alu} = \sigma^{ice}$ in Figure E.20; and (iii) the value $g_c^{adh} = 0.5$ J / m^2 of Tab. 2 is retrieved when computing the area under the traction-separation law of Figure E.20. The latter point is a basic feature of Cohesive Zone Model. The estimated area $\simeq 0.4941$ indicated in Figure E.20 is computed thanks to a Simpson quadrature rule.

References

[1] W. M. Leary, We freeze to please: A history of nasa's icing research tunnel and the quest for flight safety, Tech. rep. (2002).

[2] Y. Cao, W. Tan, Z. Wu, Aircraft icing: An ongoing threat to aviation safety, Aerospace Science and Technology 75 (2018) 353 – 385.

[3] Aircraft Icing Handbook, Civil Aviation Authority, 2000.

[4] T. Strobl, S. Storm, D. Thompson, M. Hornung, F. Thielecke, Feasibility study of a hybrid ice protection system, Journal of Aircraft 52 (6) (2015) 2064–2076.

[5] Z. Zhang, B. Chen, C. Lu, H. Wu, H. Wu, S. Jiang, G. Chai, A novel thermo-mechanical anti-icing/de-icing system using bi-stable laminate composite structures with superhydrophobic surface, Composite Structures 180 (2017) 933 – 943.

[6] X. Huang, N. Tepylo, V. Pommier-Budinger, M. Budinger, E. Bonaccurso, P. Villedieu, L. Bennani, A survey of icephobic coatings and their potential use in a hybrid coating/active ice protection system for aerospace applications, Progress in Aerospace Sciences 105 (2019) 74 – 97.

[7] S. Venna, Y. Lin, Development of self-actuating in-flight de-icing structures with power consumption considerations, in: Proceedings of the American Society of Mechanical Engineers International Mechanical Engineering Congress and Exposition, ASME Washington, DC, 2003, pp. 45–53.

[8] S. V. Venna, Y. . Lin, Mechatronic development of self-actuating in-flight deicing structures, IEEE/ASME Transactions on Mechatronics 11 (5) (2006) 585–592.

[9] S. Venna, Y.-J. Lin, G. Botura, Piezoelectric transducer actuated leading edge de-icing with simultaneous shear and impulse forces, Journal of Aircraft 44 (2) (2007) 509–515.

[10] S. Ramanathan, V. V. Varadan, V. K. Varadan, Deicing of helicopter blades using piezoelectric actuators, in: Smart Structures and Materials 2000: Smart Electronics and MEMS, Vol. 3990, International Society for Optics and Photonics, 2000, pp. 281–293.

[11] M. K. Kalkowski, T. P. Waters, E. Rustighi, Removing surface accretions with piezo-excited high-frequency structural waves, in: Active and Passive Smart Structures and Integrated Systems 2015, Vol. 9431, International Society for Optics and Photonics, 2015, p. 94311T.

[12] J. Palacios, E. Smith, Dynamic analysis and experimental testing of thin-walled structures driven by shear tube actuators, in: 46th AIAA/ASME/ASCE/AHS/ASC Structures, Structural Dynamics and Materials Conference, 2005, p. 2112.

[13] J. L. Palacios, Design, fabrication, and testing of an ultrasonic de-icing system for helicopter rotor blades, Ph.D. thesis, Pennsylvania State Univ., State College (2008).

[14] J. Palacios, E. Smith, J. Rose, et al., Investigation of an ultrasonic ice protection system for helicopter rotor blades, in: Annual Forum Proceedings-American Helicopter Society, Vol. 64, AMERICAN HELICOPTER SOCIETY, INC, 2008, p. 609.

[15] J. Palacios, E. Smith, J. Rose, R. Royer, Instantaneous de-icing of freezer ice via ultrasonic actuation, AIAA journal 49 (6) (2011) 1158–1167.

[16] J. Palacios, E. Smith, J. Rose, R. Royer, Ultrasonic de-icing of wind-tunnel impact icing, Journal of Aircraft 48 (3) (2011) 1020–1027.

[17] A. Overmeyer, J. L. Palacios, E. C. Smith, R. Royer, Rotating testing of a low-power, non-thermal ultrasonic de-icing system for helicopter rotor blades, Tech. rep., SAE Technical Paper (2011).

[18] A. Overmeyer, J. Palacios, E. Smith, Actuator bonding optimization and system control of a rotor blade ultrasonic deicing system, in: 53rd AIAA/ASME/ASCE/AHS/ASC Structures, Structural Dynamics and Materials Conference 20th AIAA/ASME/AHS Adaptive Structures Conference 14th AIAA, 2012, p. 1476.

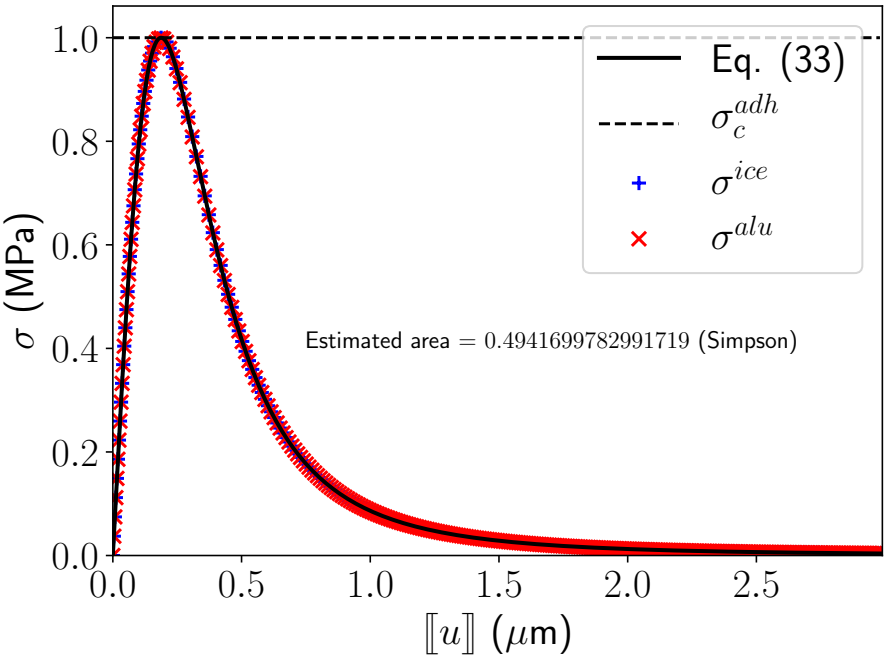

Figure E.20: Analytic traction-separation law of Eq. (33) compared with numerical ones both in ice and aluminium. Values of Tab. 2 are considered. The area under the traction-separation law matches the value $g_c^{adh} = 0.5$ J / m^2.

[19] E. Villeneuve, D. Harvey, D. Zimcik, R. Aubert, J. Perron, Piezoelectric deicing system for rotorcraft, Journal of the American Helicopter Society 60 (4) (2015) 1–12.

[20] M. Budinger, V. Pommier-Budinger, G. Napias, A. Costa da Silva, Ultrasonic ice protection systems: Analytical and numerical models for architecture tradeoff, Journal of Aircraft (0) (2016) 680–690.

[21] V. Pommier-Budinger, M. Budinger, P. Rouset, F. Dezitter, F. Huet, M. Wetterwald, E. Bonaccurso, Electromechanical resonant ice protection systems: Initiation of fractures with piezoelectric actuators, AIAA Journal 56 (11) (2018) 4400–4411.

[22] M. Budinger, V. Pommier-Budinger, L. Bennani, P. Rouset, E. Bonaccurso, F. Dezitter, Electromechanical resonant ice protection systems: Analysis of fracture propagation mechanisms, AIAA Journal 56 (11) (2018) 4412–4422.

[23] D. Li, Z. Chen, M. Shi, Effect of ultrasound on frost formation on a cold flat surface in atmospheric air flow, Experimental Thermal and Fluid Science 34 (8) (2010) 1247–1252.

[24] H. Gao, J. L. Rose, Ice detection and classification on an aircraft wing with ultrasonic shear horizontal guided waves, IEEE transactions on ultrasonics, ferroelectrics, and frequency control 56 (2) (2009) 334–344.

[25] Y. Liu, L. J. Bond, H. Hu, Ultrasonic-attenuation-based technique for ice characterization pertinent to aircraft icing phenomena, AIAA Journal (2017) 1602–1609.

[26] J. Druez, C. Phan, J. Laforte, D. Nguyen, The adhesion of glaze and rime on aluminium electrical conductors, Transactions of the Canadian Society for Mechanical Engineering 5 (4) (1978) 215–220.

[27] P. Schreurs, Fracture mechanics (lecture notes-course 4a780), Eindhoven University of Technology (2012).

[28] S. Timoshenko, Strength of Materials., Van Nostrand, 1955.

[29] L. Bennani, P. Villedieu, M. Salaun, P. Trontin, Numerical simulation and modeling of ice shedding: Process initiation, Computers & Structures 142 (2014) 15 – 27.

[30] L. Bennani, Modélisation bidimensionnelle de systèmes électrothermiques de protection contre le givre, Ph.D. thesis, ISAE-SUPAERO, Université de Toulouse (2014).

[31] L. Bennani, P. Villedieu, M. Salaun, A mixed adhesionbrittle fracture model and its application to the numerical study of ice shedding mechanisms, Engineering Fracture Mechanics 158 (2016) 59 – 80.

[32] T. Belytschko, T. Black, Elastic crack growth in finite elements with minimal remeshing, International journal for numerical methods in engineering 45 (5) (1999) 601–620.

[33] N. Moës, T. Belytschko, Extended finite element method for cohesive crack growth, Engineering Fracture Mechanics 69 (7) (2002) 813 – 833.

[34] T. Belytschko, R. Gracie, G. Ventura, A review of extended/generalized finite element methods for material modeling, Modelling and Simulation in Materials Science and Engineering 17 (4) (2009) 043001.

[35] M. E. Gurtin, P. Podio-Guidugli, Configurational forces and the basic laws for crack propagation, Journal of the Mechanics and Physics of Solids 44 (6) (1996) 905 – 927.

[36] E. Gürses, C. Miehe, A computational framework of three-dimensional configurational-force-driven brittle crack propagation, Computer Methods in Applied Mechanics and Engineering 198 (15) (2009) 1413 – 1428.
[37] T. Rabczuk, Computational methods for fracture in brittle and quasi-brittle solids: state-of-the-art review and future perspectives, ISRN Applied Mathematics 2013 (2013).
[38] D. Dugdale, Yielding of steel sheets containing slits, Journal of the Mechanics and Physics of Solids 8 (2) (1960) 100 – 104.
[39] G. Barenblatt, The mathematical theory of equilibrium cracks in brittle fracture, Vol. 7 of Advances in Applied Mechanics, Elsevier, 1962, pp. 55 – 129.
[40] M. Alfano, F. Furgiuele, A. Leonardi, C. Maletta, G. H. Paulino, Cohesive zone modeling of mode i fracture in adhesive bonded joints, in: Key Engineering Materials, Vol. 348, Trans Tech Publ, 2007, pp. 13–16.
[41] G. Francfort, J.-J. Marigo, Revisiting brittle fracture as an energy minimization problem, Journal of the Mechanics and Physics of Solids 46 (8) (1998) 1319 – 1342.
[42] B. Bourdin, G. A. Francfort, J.-J. Marigo, The variational approach to fracture, Journal of elasticity 91 (1-3) (2008) 5–148.
[43] W. Lu, H.-M. Heyn, R. Lubbad, S. Lset, A large scale simulation of floe-ice fractures and validation against full-scale scenario, International Journal of Naval Architecture and Ocean Engineering 10 (3) (2018) 393 – 402.
[44] S. Jiménez, R. Duddu, J. Bassis, An updated-lagrangian damage mechanics formulation for modeling the creeping flow and fracture of ice sheets, Computer Methods in Applied Mechanics and Engineering 313 (2017) 406 – 432.
[45] A. Samak, P. Rampal, S. Bouillon, E. lason, Parallel implementation of a lagrangian-based model on an adaptive mesh in c++: Application to sea-ice, Journal of Computational Physics 350 (2017) 84 – 96.
[46] I. Konuk, A. Gürtner, S. Yu, A cohesive element framework for dynamic ice-structure interaction problemspart ii: Implementation, in: ASME 2009 28th International Conference on Ocean, Offshore and Arctic Engineering, American Society of Mechanical Engineers, 2009, pp. 185–193.
[47] A. Gürtner, Experimental and numerical investigations of ice-structure interaction, Ph.D. thesis, Norwegian University of Science and Technology (2009).
[48] P. G. Bergan, G. Cammaert, G. Skeie, V. Tharigopula, On the potential of computational methods and numerical simulation in ice mechanics, in: IOP Conference Series: Materials Science and Engineering, Vol. 10, IOP Publishing, 2010, p. 012102.
[49] H. Sommerwerk, P. Horst, Analysis of the mechanical behavior of thin ice layers on structures including radial cracking and de-icing, Engineering Fracture Mechanics 182 (2017) 400 – 424.
[50] M. M. Riahi, D. Marceau, C. Laforte, J. Perron, The experimental/numerical study to predict mechanical behaviour at the ice/aluminium interface, Cold Regions Science and Technology 65 (2) (2011) 191 – 202.
[51] C. Miehe, M. Hofacker, F. Welschinger, A phase field model for rate-independent crack propagation: Robust algorithmic implementation based on operator splits, Computer Methods in Applied Mechanics and Engineering 199 (45) (2010) 2765 – 2778.
[52] C. Miehe, F. Welschinger, M. Hofacker, Thermodynamically consistent phase-field models of fracture: Variational principles and multi-field fe implementations, International Journal for Numerical Methods in Engineering 83 (10) (2010) 1273–1311.
[53] M. J. Borden, C. V. Verhoosel, M. A. Scott, T. J. Hughes, C. M. Landis, A phase-field description of dynamic brittle fracture, Computer Methods in Applied Mechanics and Engineering 217-220 (2012) 77 – 95.
[54] C. V. Verhoosel, R. de Borst, A phase-field model for cohesive fracture, International Journal for Numerical Methods in Engineering 96 (1) (2013) 43–62.
[55] M. J. Borden, T. J. Hughes, C. M. Landis, C. V. Verhoosel, A higher-order phase-field model for brittle fracture: Formulation and analysis within the isogeometric analysis framework, Computer Methods in Applied Mechanics and Engineering 273 (2014) 100 – 118.
[56] M. A. Msekh, N. Cuong, G. Zi, P. Areias, X. Zhuang, T. Rabczuk, Fracture properties prediction of clay/epoxy nanocomposites with interphase zones using a phase field model, Engineering Fracture Mechanics 188 (2018) 287 – 299.
[57] P. Areias, T. Rabczuk, M. Msekh, Phase-field analysis of finite-strain plates and shells including element subdivision, Computer Methods in Applied Mechanics and Engineering 312 (2016) 322 – 350.
[58] A. A. Griffith, Vi. the phenomena of rupture and flow in solids, Philosophical transactions of the royal society of london. Series A, containing papers of a mathematical or physical character 221 (582-593) (1921) 163–198.
[59] J.-Y. Wu, A unified phase-field theory for the mechanics of damage and quasi-brittle failure, Journal of the Mechanics and Physics of Solids 103 (2017) 72 – 99.
[60] L. Ambrosio, V. M. Tortorelli, Approximation of functional depending on jumps by elliptic functional via t-convergence, Communications on Pure and Applied Mathematics 43 (8) (1990) 999–1036.
[61] L. Ambrosio, V. Tortorelli, On the approximation of free discontinuity problems, BOLLETTINO DELL'UNIONE MATEMATICA ITALIANA. B 6 (1) (1992) 105–123.
[62] A. Braides, et al., Approximation of free-discontinuity problems, no. 1694, Springer Science & Business Media, 1998.
[63] A. Braides, G. Dal Maso, A. Garroni, Variational formulation of softening phenomena in fracture mechanics: The one-dimensional case, Archive for Rational Mechanics and Analysis 146 (1) (1999) 23–58.
[64] L. Ambrosio, N. Fusco, D. Pallara, Functions of bounded variation and free discontinuity problems, Vol. 254, Clarendon Press Oxford, 2000.
[65] A. Braides, Gamma-convergence for Beginners, Vol. 22, Clarendon Press, 2002.
[66] A. Braides, Chapter 2 a handbook of gamma-convergence, Vol. 3 of Handbook of Differential Equations: Stationary Partial Differential Equations, North-Holland, 2006, pp. 101 – 213.
[67] G. Dal Maso, An introduction to Gamma-convergence, Vol. 8, Springer Science & Business Media, 2012.
[68] T. Linse, P. Hennig, M. Kästner, R. de Borst, A convergence study of phase-field models for brittle fracture, Engineering Fracture Mechanics 184 (2017) 307 – 318.
[69] C. Miehe, L.-M. Schänzel, H. Ulmer, Phase field modeling of fracture in multi-physics problems. part i. balance of crack surface and failure criteria for brittle crack propagation in thermo-elastic solids, Computer Methods in Applied Mechanics and Engineering 294 (2015) 449 – 485.
[70] K. Pham, H. Amor, J.-J. Marigo, C. Maurini, Gradient damage models and their use to approximate brittle fracture, International Journal of

Damage Mechanics 20 (4) (2011) 618–652.
[71] B. Bourdin, J.-J. Marigo, C. Maurini, P. Sicsic, Morphogenesis and propagation of complex cracks induced by thermal shocks, Phys. Rev. Lett. 112 (2014) 014301.
[72] E. Tanné, T. Li, B. Bourdin, J.-J. Marigo, C. Maurini, Crack nucleation in variational phase-field models of brittle fracture, Journal of the Mechanics and Physics of Solids 110 (2018) 80 – 99.
[73] J.-Y. Wu, V. P. Nguyen, A length scale insensitive phase-field damage model for brittle fracture, Journal of the Mechanics and Physics of Solids 119 (2018) 20 – 42.
[74] Frémond, M, Adhérence des solides, Journal de mécanique théorique et appliquée 6 (3) (1987) 383–407.
[75] G. Sih, J. Rice, Plane problems of cracks in dissimilar materials, J. Appl. Mech 32 (1965) 418–423.
[76] P. Archer, V. Gupta, Measurement and control of ice adhesion to aluminum 6061 alloy, Journal of the Mechanics and Physics of Solids 46 (10) (1998) 1745 – 1771.
[77] X.-P. Xu, A. Needleman, Numerical simulations of fast crack growth in brittle solids, Journal of the Mechanics and Physics of Solids 42 (9) (1994) 1397 – 1434.
[78] A. Caporale, R. Luciano, E. Sacco, Micromechanical analysis of interfacial debonding in unidirectional fiber-reinforced composites, Computers & Structures 84 (31) (2006) 2200 – 2211.
[79] C. Panagiotopoulos, V. Mantič, T. Roubíček, Bem implementation of energetic solutions for quasistatic delamination problems, in: Advances in Boundary Element Techniques XII (BeTeq 2011) EL Albuquerque, MH Aliabadi (Eds.), Engineering Conferences Ltd., Eastleigh, 2011, pp. 261–268.
[80] T. Roubíček, V. Mantič, C. G. Panagiotopoulos, Quasistatic mixed-mode delamination model, Disc. Cont. Dynam. Syst., Ser. S 6 (2013) 591–610.
[81] R. Vodička, V. Mantič, T. Roubíček, Energetic versus maximally-dissipative local solutions of a quasi-static rate-independent mixed-mode delamination model, Meccanica 49 (12) (2014) 2933–2963.
[82] A. Turon, C. Dávila, P. Camanho, J. Costa, An engineering solution for mesh size effects in the simulation of delamination using cohesive zone models, Engineering Fracture Mechanics 74 (10) (2007) 1665 – 1682.
[83] P. Gilormini, J. Diani, Testing some implementations of a cohesive-zone model at finite strain, Engineering Fracture Mechanics 148 (2015) 97 – 109.
[84] R. Dimitri, M. Trullo, L. D. Lorenzis, G. Zavarise, Coupled cohesive zone models for mixed-mode fracture: A comparative study, Engineering Fracture Mechanics 148 (2015) 145 – 179.
[85] F. Hirsch, M. Kästner, Microscale simulation of adhesive and cohesive failure in rough interfaces, Engineering Fracture Mechanics 178 (2017) 416 – 432.
[86] X. Zhang, S. W. Sloan, C. Vignes, D. Sheng, A modification of the phase-field model for mixed mode crack propagation in rock-like materials, Computer Methods in Applied Mechanics and Engineering 322 (2017) 123 – 136.
[87] B. Bourdin, G. Francfort, J.-J. Marigo, Numerical experiments in revisited brittle fracture, Journal of the Mechanics and Physics of Solids 48 (4) (2000) 797 – 826.
[88] U. Nakaya, Visco-elastic properties of snow and ice in greenland ice cap, Journal of the Faculty of Science, Hokkaido University. Ser. 2, Physics 5 (3) (1958) 119–164.
[89] R. Scavuzzo, M. L. Chu, Structural properties of impact ices accreted on aircraft structures (1987).
[90] P. Gammon, H. Kiefte, M. Clouter, W. Denner, Elastic constants of artificial and natural ice samples by brillouin spectroscopy, Journal of glaciology 29 (103) (1983) 433–460.
[91] J. Petrovic, Review mechanical properties of ice and snow, Journal of materials science 38 (1) (2003) 1–6.
[92] S. Struggl, J. Korak, C. Feyrer, A basic approach for wing leading deicing by smart structures, in: Sensors and Smart Structures Technologies for Civil, Mechanical, and Aerospace Systems 2011, Vol. 7981, International Society for Optics and Photonics, 2011, p. 79815L.
[93] A. Mohamed, M. Farzaneh, An experimental study on the tensile properties of atmospheric ice, Cold regions science and technology 68 (3) (2011) 91–98.
[94] A. Work, Y. Lian, A critical review of the measurement of ice adhesion to solid substrates, Progress in Aerospace Sciences 98 (2018) 1 – 26.
[95] S. Ramtani, Y. Berthaud, J. Mazars, Orthotropic behavior of concrete with directional aspects: modelling and experiments, Nuclear Engineering and Design 133 (1) (1992) 97 – 111.
[96] C. Geuzaine, J.-F. Remacle, Gmsh: A 3-d finite element mesh generator with built-in pre-and post-processing facilities, International journal for numerical methods in engineering 79 (11) (2009) 1309–1331.
[97] V. Mantič, L. Távara, A. Blázquez, E. Graciani, F. París, A linear elastic-brittle interface model: application for the onset and propagation of a fibre-matrix interface crack under biaxial transverse loads, International Journal of Fracture 195 (1-2) (2015) 15–38.
[98] H. Brezis, Functional analysis, Sobolev spaces and partial differential equations, Springer Science & Business Media, 2010.